

1 **Uncertainty quantification of ocean parameterizations:**
2 **application to the K-Profile-Parameterization for**
3 **penetrative convection**

4 **A. N. Souza¹, G. L. Wagner¹, A. Ramadhan¹, B. Allen¹, V. Churavy¹, J.**
5 **Schloss¹, J. Campin¹, C. Hill¹, A. Edelman¹, J. Marshall¹, G. Flierl¹, R.**
6 **Ferrari¹**

7 ¹Massachusetts Institute of Technology, 77 Massachusetts Ave, Cambridge, MA 02139, United States

8 **Key Points:**

- 9 • A Bayesian methodology is used to probe turbulence parameterizations and bet-
10 ter understand their biases and uncertainties.
11 • Parameterization parameter distributions, learned using high-resolution simula-
12 tions, should be used as prior distributions for climate modeling studies.

Corresponding author: A. N. Souza, andrenogueirasouza@gmail.com

13 **Abstract**

14 Parameterizations of unresolved turbulent processes often compromise the fidelity of large-
 15 scale ocean models. In this work, we argue for a Bayesian approach to the refinement
 16 and evaluation of turbulence parameterizations. Using an ensemble of large eddy sim-
 17 ulations of turbulent penetrative convection in the surface boundary layer, we demon-
 18 strate the method by estimating the uncertainty of parameters in the convective limit
 19 of the popular ‘K-Profile Parameterization’. We uncover structural deficiencies and pro-
 20 pose an alternative scaling that overcomes them.

21 **Plain Language Summary**

22 Climate projections are often compromised by significant uncertainties which stem
 23 from the representation of physical processes that cannot be resolved – such as clouds
 24 in the atmosphere and turbulent swirls in the ocean – but which have to be parameterised.
 25 We propose a methodology for improving parameterizations in which they are tested against,
 26 and tuned to, high-resolution numerical simulations of subdomains that represent them
 27 more completely. A Bayesian methodology is used to calibrate the parameterizations against
 28 the highly resolved model, to assess their fidelity and identify shortcomings. Most im-
 29 portantly, the approach provides estimates of parameter uncertainty. While the method
 30 is illustrated for a particular parameterization of boundary layer mixing, it can be ap-
 31 plied to any parameterization.

32 **1 Introduction**

33 Earth System Models (ESMs) require parameterizations for processes that are too
 34 small to resolve. Uncertainties arise both due to deficiencies in the scaling laws encoded
 35 in the parameterizations and the nonlinear interactions with resolved model components,
 36 sometimes leading to unanticipated and unphysical results. The first challenge can be
 37 addressed by improving the representation of the unresolved physics (e.g. Schneider, Lan,
 38 et al., 2017), while the second requires ‘tuning’ of the parameterizations when implemented
 39 in the full ESM (e.g. Hourdin et al., 2017). In this paper, we illustrate how to leverage
 40 recent advances in computation and uncertainty quantification to make progress toward
 41 the first challenge. Our focus will be on oceanic processes, but the approach can be ap-
 42 plied to any ESM parameterization, provided that a high-resolution submodel can be con-
 43 structed.

44 The traditional approach to the formulation of parameterizations of subgrid-scale
 45 processes is to derive scaling laws that relate the net effect of such processes to variables
 46 resolved by the ESMs. These scaling laws are then tested with either field observations (e.g.
 47 Price et al., 1986; Large et al., 1994), laboratory experiments (e.g. Deardorff et al., 1980;
 48 Cenedese et al., 2004) or results from a high resolution simulations (e.g. Wang et al., 1996;
 49 Harcourt, 2015; Reichl et al., 2016; Li & Fox-Kemper, 2017). Rarely are parameteriza-
 50 tions tested over a wide range of possible scenarios due to the logistical difficulty and
 51 high cost of running many field experiments, the time necessary to change laboratory
 52 setups, and computational demand. The computational limitations have become much
 53 less severe over the last few years through a combination of new computer architectures
 54 such as Graphic Processing Units (GPUs; Besard et al., 2019), new languages that take
 55 advantage of these architectures (e.g Julia; Bezanson et al., 2017) and improved Large
 56 Eddy Simulation (LES) algorithms (Sullivan & Patton, 2011; Verstappen, 2018). Mod-
 57 ern computational resources have opened up the possibility of running libraries of LES
 58 simulations to explore a vast range of possible scenarios. This paper discusses how such
 59 computational advances can be applied to assess parameterizations in ocean models.

60 LES simulations alone are not sufficient to formulate parameterizations. Statisti-
 61 cal methods are needed to extract from the LES solutions the functional relationships

62 between small-scale processes and coarse variables available in ESMs. A common approach
 63 is to rely on well-established scaling laws and use the LES solutions to constrain the non-
 64 dimensional parameters that cannot be determined from first principles. In this approach,
 65 only a few LES simulations are necessary to find the optimal parameter values. How-
 66 ever, it is rare that scaling laws and associated parameterizations perfectly capture the
 67 functional dependencies of large-scale variables – if they did, they would be referred to
 68 as solutions rather than parameterizations. In general, it is necessary to run a large en-
 69 semble of LES simulations to estimate optimal parameter values and test whether those
 70 values hold for different scenarios, thereby supporting the functional dependencies.

71 State-estimation, which has a long tradition in geophysics (Wunsch, 2006), has been
 72 used to constrain parameter values. A loss function is chosen to quantify the mismatch
 73 between the prediction of the parameterization and observations. Uncertain parameters
 74 are then adjusted to minimize the loss function. One can also estimate the standard de-
 75 viation around the optimal values by computing the Hessian of the loss function (Thacker,
 76 1989; Sraj et al., 2014).

77 An alternative approach, based on the seminal work of (Bayes, 1763) and its mod-
 78 ern incarnation (Jaynes, 2003), is arguably better suited to constrain the transfer prop-
 79 erties of turbulent processes. The Bayesian method allows one to estimate the entire joint
 80 probability distribution of all parameters. The method is a crucial extension over state-
 81 estimation, because the statistics of turbulent processes are generally far from Gaussian (Frisch,
 82 1995) and thus are not fully characterized by the first and second moments alone. In the
 83 Bayesian approach, one defines a prior parameter distribution, based on physical con-
 84 siderations, and a ‘likelihood function’ which measures the mismatch between the pa-
 85 rameterized prediction and the LES simulation. Based on this information, Bayes’ for-
 86 mula shows how to compute the posterior distribution of the parameters consistent with
 87 the LES simulations and the parameterization. If the posterior distribution is narrow
 88 and peaked, then one can conclude that a unique set of parameters can be identified which
 89 can reproduce all LES results. In this limit, the Bayesian approach does not provide more
 90 information than state-estimation. However, the power of Bayes’ formula is that it can
 91 reveal distinct parameter regimes, the existence of multiple maxima, relationships be-
 92 tween parameters, and the likelihood of parameter values relative to optimal ones.

93 The Bayesian approach can also be used to test the functional dependence of the
 94 parameterization on large-scale variables. One estimates the posterior distribution on
 95 subsets of the LES simulations run for different scenarios. If the posterior probabilities
 96 for the different scenarios do not overlap, the functional form of the parameterization
 97 must be rejected. We will illustrate how this strategy can be used to improve the for-
 98 mulation of a parameterization.

99 Bayesian methods are particularly suited to constrain ESM parameterizations of
 100 subgrid-scale ocean processes. Most of these processes, such as boundary layer or geostrophic
 101 turbulence, are governed by well understood fluid dynamics and thermodynamics. Thus
 102 LES simulations provide credible solutions for the physics. The atmospheric problem is
 103 quite different where leading order subgrid-scale processes such as cloud microphysics
 104 are governed by poorly understood physics that may not be captured by LES simula-
 105 tions.

106 In this paper, we will apply Bayesian methods to constrain and improve a param-
 107 eterization for the surface boundary layer turbulence that develops when air-sea fluxes
 108 cool the ocean. LES simulations that resolve all the relevant physics will be used as ground-
 109 truth to train the parameterization. Our paper is organized as follows: In section 2 we
 110 describe the physical setup and the LES model. In section 3 we introduce Bayesian pa-
 111 rameter estimation for the parameters in the K-Profile Parameterization (KPP). We then
 112 perform the parameter estimation in the regime described by section 2 and show how

113 the Bayesian approach provides insight on how to improve the KPP parameterization.
 114 Finally, we end with a discussion in section 4.

115 **2 Large eddy simulations and K-Profile Parameterization of penetra-** 116 **tive convection**

117 During winter, high latitude cooling induces near-surface mixing by convection which
 118 generates a ‘mixed layer’ of almost uniform temperature and salinity which can reach
 119 depths of hundreds of meters: - see (Marshall & Schott, 1999) for a review. At the base
 120 of the mixed layer, convective plumes can penetrate further into the stratified layer be-
 121 low – called the ‘entrainment layer’ – where plume-driven turbulent mixing between the
 122 mixed layer and stratification below cools the boundary layer. This process, in which the
 123 layer is cooled both at the surface and by turbulent mixing from the entrainment layer
 124 below, is called penetrative convection. Here we evaluate the ability of the K-Profile Pa-
 125 rameterization (Large et al., 1994) to capture penetrative convection by comparing pre-
 126 dictions based on it against large eddy simulations (LES) of idealized penetrative con-
 127 vection into a resting stratified fluid. It provides the context in which we outline the Bayesian
 128 approach to parameter estimation which we advocate.

129 **2.1 Penetrative convection into a resting stratified fluid**

We suppose a constant surface cooling $Q_h > 0$ to a resting, linearly stratified bound-
 ary layer with the initial state

$$\mathbf{u}|_{t=0} = 0 \text{ and } b|_{t=0} = 20\alpha g + N^2 z + \mathcal{N}(0, 10^{-10}\alpha g) \exp(4z/L_z), \quad (1)$$

where $z \in [-L_z, 0]$, $\mathbf{u} = (u, v, w)$ is the resolved velocity field simulated by LES, b is
 buoyancy, N^2 is the initial vertical buoyancy gradient, and $\mathcal{N}(0, \alpha g 10^{-10})$ is a Gaussian
 white noise process added to induce a transition to turbulence. The surface buoyancy
 flux Q_b is related to the imposed surface cooling Q_h , which has units W m^{-2} , via

$$Q_b = \frac{\alpha g}{\rho_{\text{ref}} c_p} Q_h, \quad (2)$$

130 where $\alpha = 2 \times 10^{-4} (\text{°C})^{-1}$ is the thermal expansion coefficient (assumed constant),
 131 $g = 9.81 \text{ m s}^{-2}$ is gravitational acceleration, $\rho_{\text{ref}} = 1035 \text{ kg m}^{-3}$ is a reference density,
 132 and $c_p = 3993 \text{ J/(kg °C)}$ is the specific heat capacity. Our software and formulation of
 133 the large eddy simulation model is discussed in Appendix A.

Results from a large eddy simulation of turbulent penetrative convection in a do-
 main $L_x = L_y = L_z = 100$ meters and $256 \times 256 \times 512$ grid cells, respectively, is pre-
 sented in Figure 1. The resulting horizontally averaged temperature profiles are not af-
 fected by the domain size. The left panel shows the three-dimensional temperature field
 $\theta = \theta_0 + b/\alpha g$ associated with the buoyancy b , where $\theta_0 = 20^\circ\text{C}$ is the surface tem-
 perature at $z = 0$. The right panel shows the horizontally averaged buoyancy profile

$$\bar{b}(z, t) \equiv \frac{1}{L_x L_y} \int_0^{L_x} \int_0^{L_y} b(x, y, z, t) dx dy. \quad (3)$$

134 The visualization reveals the two-part boundary layer produced by penetrative con-
 135 vection: close to the surface, cold and dense convective plumes organized by surface cool-
 136 ing sink and mix ambient fluid, producing a well-mixed layer that deepens in time. Be-
 137 low the mixed layer, the momentum carried by sinking convective plumes leads them to
 138 overshoot their level of neutral buoyancy (nominally, the depth of the mixed layer), ‘pen-
 139 etrating’ the stably stratified region below the surface mixed layer and generating the
 140 strongly stratified entrainment layer. The total depth of the boundary layer is h and in-
 141 cludes the mixed layer and the entrainment layer of thickness Δh . Turbulent fluxes are
 142 assumed negligible below $z = -h$.

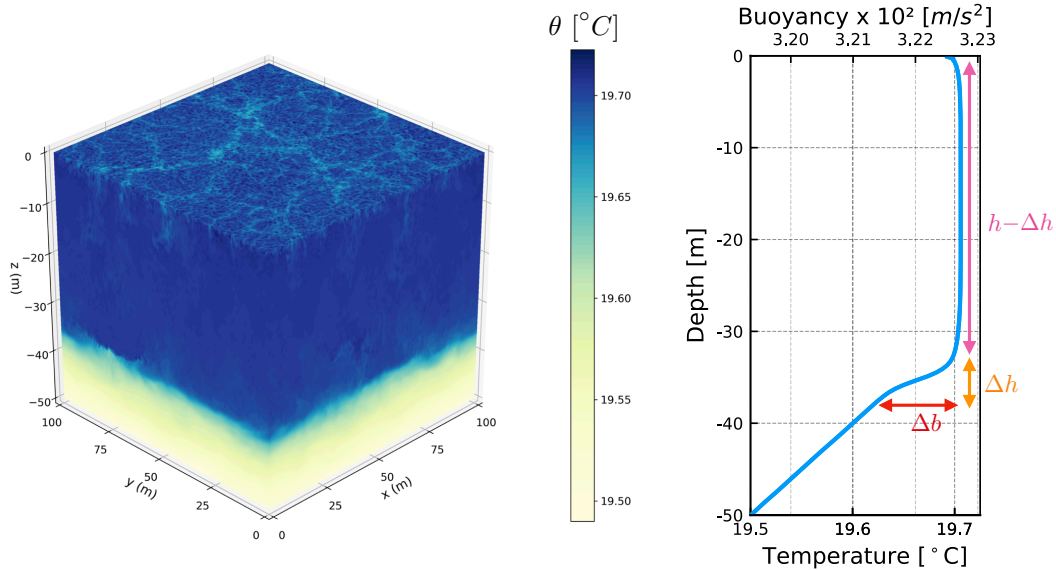


Figure 1. A 3D simulation of the LES model of the Boussinesq equations and its horizontal average at $t = 2$ days. The Δh region of the figure on the right corresponds to the entrainment layer, $h - \Delta h$ corresponds to the mixed layer, and h corresponds to the boundary layer depth.

In figure 2 we show the evolution of $h(t)$ defined as the first depth from the bottom where the stratification is equal to a weighted average of the maximum stratification and the initial stratification¹. The dotted line confirms that the evolution after an initial transient is best fit by the formula,

$$h \simeq \sqrt{3.0 \frac{Q_b}{N^2} t}, \quad (4)$$

143 where N^2 is the initial stratification and the numerical factor is a best-fit parameter.

Equation 4 is easily understood through dimensional considerations (up to prefactors), but more information flows from an analysis of the horizontally-averaged buoyancy equation,

$$\partial_t \bar{b} = -\partial_z (\overline{wb} + \overline{q^{(z)}}), \quad (5)$$

where \bar{b} is the horizontally averaged buoyancy, \overline{wb} is the horizontally averaged vertical advective flux and $\overline{q^{(z)}}$ is the horizontally averaged vertical diffusive flux. Integrating the equation in time between $t' = 0$ and some later time $t' = t$, and in the vertical between the surface, where $q^{(z)} = -Q_b$, and the base of the entrainment layer where all turbulent fluxes vanish, one finds,

$$\int_{-h}^0 [\bar{b}(z, t) - \bar{b}(z, 0)] dz = -Q_b t. \quad (6)$$

¹ The weights are $2/3$ for the initial stratification N^2 and $1/3$ for the maximum stratification N_m^2 so that h satisfies $\partial_z \bar{b}(-h) = 2N_b^2/3 + N_m^2/3$. This guarantees that h is a depth where the local stratification lies between the background stratification and the maximum stratification since it is defined as the *first* depth starting from the bottom that satisfies such a criteria.

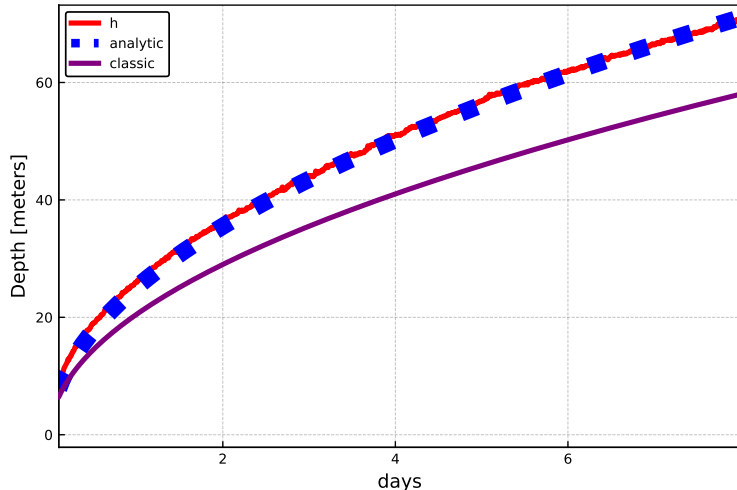


Figure 2. Boundary layer depth and its evolution in time after initial transients. The blue squares are the analytic scaling 4, the red line is an estimate of the boundary layer depth directly from the LES (described in the text), and the purple line is the classic scaling which ignores the entrainment layer 8.

Substituting $\bar{b}(z, 0) = b_0 + N^2(z + h)$ and $\bar{b}(z, t) = b_0 + \Delta b$, an approximation of the profile shown in Fig. 1b except at very early times in the simulation, yields

$$\frac{1}{2}N^2h^2 - h\Delta b = Q_b t. \quad (7)$$

144 The first term on the left of equation 7 describes boundary layer deepening due to buoy-
 145 ancy loss at the surface, while the second term corresponds to the further cooling caused
 146 by turbulent mixing in the entrainment layer. Other authors have also arrived at a simi-
 147 lar expression for the boundary layer depth upon taking into account turbulent entrain-
 148 ment. See, for example, Appendix F in (Van Roekel et al., 2018).

Ignoring turbulent mixing in the entrainment layer, i.e. setting $\Delta b = 0$, yields the deepening rate

$$h = \sqrt{2.0 \frac{Q_b}{N^2} t}, \quad (8)$$

149 which differs by roughly 20% from the best fit expression 4 due to the effects of turbu-
 150 lent mixing in the entrainment layer. Equation 8 is the deepening rate associated with
 151 a convective adjustment parameterization and is known as the empirical law of free con-
 152 vection. We now review how these processes are represented in the KPP model.

153 2.2 The K-Profile Parameterization of penetrative convection

In penetrative convection in a horizontally-periodic domain, the K-Profile Parameterization models the horizontally-averaged temperature profile, $\bar{\theta}(z, t)$ with the coupled equations

$$\partial_t T = -\partial_z F(T, h; \mathbf{C}) \quad (9)$$

$$0 = \mathcal{D}(T, h; \mathbf{C}), \quad (10)$$

154 where $T(z, t)$ is the modeled temperature meant to approximate $\bar{\theta}(z, t)$, $h(t)$ is the bound-
 155 ary layer depth, $\mathbf{C} = \{C^S, C^N, C^D, C^H\}$ is a set of free parameters, $F(T, h; \mathbf{C})$ is the

156 parameterized temperature flux, and $\mathcal{D}(T, h; \mathbf{C})$ is a nonlinear constraint that determines
 157 the boundary layer depth at each time t . Our formulation, which isolates the four free
 158 parameters $\{C^S, C^N, C^D, C^H\}$, is superficially different but mathematically equivalent
 159 to the formulation in (Large et al., 1994) (see Appendix C for details). Finally, we em-
 160 phasize that the K-Profile parameterization is deemed successful only if it accurately mod-
 161 els the evolution of the entire observed temperature profile $\bar{\theta}(z, t)$, rather than, say, the
 162 boundary layer depth or the buoyancy jump across the base of the mixed layer.

The K-Profile Parameterization (KPP) represents F through the sum of a down-
 gradient flux and a non-local flux term (Large et al., 1994),

$$F = - \underbrace{C^D \delta^{1/3} w_* h \frac{z}{h} \left(1 + \frac{z}{h}\right)^2}_{\equiv K} \partial_z T + \underbrace{C^N Q^\theta \frac{z}{h} \left(1 + \frac{z}{h}\right)^2}_{\equiv \Phi}, \quad (11)$$

163 for $-h \leq z \leq 0$ and 0 otherwise, and $\delta = \min\{C^S, z/h\}$. Here $w_* = (Q_b h)^{1/3}$ is the
 164 convective turbulent velocity scale, h is the boundary layer depth, $\frac{z}{h} \left(1 + \frac{z}{h}\right)^2$ is the ‘K-
 165 profile’ shape function (K is the namesake downgradient diffusivity of the K-Profile Pa-
 166 rameterization) and Φ is a ‘non-local’ flux term that models convective boundary layer
 167 fluxes not described by downgradient diffusion.

The KPP model estimates the boundary layer depth h using the nonlinear constraint
 (10). The boundary layer geometry introduced in the right panel of figure 1 motivates
 the form of nonlinear constraint. The jump in buoyancy, Δb , is the difference between
 the buoyancy in the mixed layer and the base of the entrainment region. The buoyancy
 jump may thus be written in terms of the entrainment region thickness, Δh , and the en-
 trainment region buoyancy gradient, N_e^2 , as $\Delta b = N_e^2 \Delta h$. Using the plume theory out-
 lined in Appendix B to motivate the scaling $\Delta h \propto w_*/N_e$, we thus find

$$\tilde{C}^H = \frac{\Delta b}{w_* N_e} \quad (12)$$

168 for some universal proportionality constant \tilde{C}^H . KPP posits that the boundary layer depth
 169 h is the first such depth from the surface at which equation 12 holds.

Large et al. (1994) estimate the mixed layer buoyancy with an average over the ‘sur-
 face layer’, $\frac{1}{C^S h} \int_{-C^S h}^0 B(z) dz$ where $B = \alpha g T$, and $0 < C^S < 1$ is a free parameter
 that defines the fractional depth of the surface layer relative to the total boundary layer
 depth, h . The buoyancy jump becomes, therefore

$$\Delta b = \frac{1}{C^S h} \int_{-C^S h}^0 B(z) dz - B(-h). \quad (13)$$

Large et al. (1994) then express the stratification in the entrainment region, N_e , in terms
 of the stratification at the base of the boundary layer, such that

$$N_e \propto \sqrt{\max[0, \partial_z B(-h)]}. \quad (14)$$

The scaling in equation 14 introduces a new free parameter in addition to \tilde{C}^H ; however
 because this free parameter is not independent from \tilde{C}^H , we combine the two into a new
 free parameter C^H , which we call the ‘mixing depth parameter’. To prevent division by
 zero, the small dimensional constant $10^{-11} \text{m}^2 \text{s}^{-2}$ is added to the demoninator of equa-
 tion 12 (Griffies et al., 2015). Combining equations 12, 13 and 14, we can write

$$0 = C^H - \frac{\frac{1}{C^S h} \int_{-C^S h}^0 B(z) dz - B(-h)}{(h Q_b)^{1/3} \sqrt{\max[0, \partial_z B(-h)] + 10^{-11} \text{m}^2 \text{s}^{-2}}}. \quad (15)$$

170 Equation 15 is the implicit nonlinear constraint in equation 10 that determines the
 171 boundary layer depth, h . In Appendix B we discuss the physical content of equation 15
 172 for the case of penetrative convection.

173 The boundary layer depth criteria in equation 15 is often referred to as the bulk
 174 Richardson number criteria, because in mechanically forced turbulence the denomina-
 175 tor is replaced by an estimate of the mean shear squared and C^H becomes a critical bulk
 176 Richardson number (Large et al., 1994). In penetrative convection there is no mean shear
 177 and C^H is not a Richardson number. See Appendix C for more details.

The representation of penetrative convection in KPP has four free parameters: the surface layer fraction C^S , the flux scalings C^N and C^D in equation 11, and the mixing depth parameter C^H in equation 15. Ranges for their default values are reported in (Large et al., 1994). We choose reference parameters within those ranges as

$$(C^S, C^N, C^D, C^H) = (0.1, 6.33, 1.36, 0.96). \quad (16)$$

178 These parameters are *not* the original set of independent parameters proposed by Large
 179 et al. (1994), but rather algebraic combinations thereof. Nevertheless, we emphasize that
 180 our formulation is mathematically identical to that proposed by Large et al. (1994). The
 181 mapping between the current set of parameters and the original are one-to-one, hence
 182 no information is lost in transforming from the current set of parameters to the origi-
 183 nal ones, see Appendix C for details. With regard to the numerical implementation, we
 184 do not use enhanced diffusivity as explained in the appendices of Large et al. (1994). Our
 185 objective is to calibrate the free parameters $\mathbf{C} = (C^S, C^N, C^D, C^H)$ by comparing KPP
 186 temperature profiles $T(z, t; \mathbf{C})$ with the LES output $\bar{\theta}(z, t)$.

187 3 Model calibration against LES solutions

We outline a Bayesian method for optimizing and estimating the uncertainty of the four free parameters through a comparison of the parameterization solution for $T(z, t; \mathbf{C})$ and the output $\bar{\theta}(z, t)$ of the LES simulations. First we introduce a loss function to quantify the parameterization-LES difference,

$$\mathcal{L}(\mathbf{C}) = \max_{t \in [t_1, t_2]} \left\{ \frac{1}{L_z} \int_{-L_z}^0 [T(z, t; \mathbf{C}) - \bar{\theta}(z, t)]^2 dz \right\}. \quad (17)$$

188 We choose the square error in space to reduce the sensitivity to vertical fluctuations in
 189 the temperature profile. We take the maximum value of the squared error in time for
 190 $t \in [t_1, t_2]$ to guarantee that the temperature profile never deviates too far from the LES
 191 simulation at each instant in time. The parameterization is taken to be the KPP model
 192 given by equations 9 through 15, and the data are the horizontally averaged LES out-
 193 put. The initial time t_1 is chosen after the initial transition to turbulence of the LES sim-
 194 ulations.

195 A natural way to extend the concept of loss functions to account for parameter un-
 196 certainty is to introduce a likelihood function for the parameters. Similar to how the form
 197 of the loss function is critical to the estimation of optimal parameters, the form of the
 198 likelihood function is critical for estimating the parameter uncertainties. The likelihood
 199 function quantifies what we mean by “good” or “bad” parameter choices. The Bayesian
 200 method uses this information to estimate parameter uncertainties. These estimates are
 201 only as good as the choice of likelihood function, much like optimal parameters are only
 202 as good as the choice of the loss function. See, for example, van Lier-Walqui, Vukicevic,
 203 & Posselt, 2012; Zedler, Kanschat, Korty, & Hoteit, 2012; Urrego-Blanco, Urban, Hunke,
 204 Turner, & Jeffery, 2016; Sraj, Zedler, Knio, Jackson, & Hoteit, 2016; Schneider, Teix-
 205 eira, et al., 2017; Nadiga, Jiang, & Livescu, 2019; Morrison, van Lier-Walqui, Kumjian,
 206 & Prat, 2020 for definitions of likelihoods in various geophysical / fluid dynamical con-
 207 texts. In Appendix D we discuss in detail the rationale for the choices made in this pa-
 208 per.

Following Schneider, Lan, et al. (2017) we introduce the likelihood function as the probability that parameter values explain the data $\mathbb{P}(\text{data}|\mathbf{C})$, as:

$$\mathbb{P}(\text{data}|\mathbf{C}) \propto \exp\left(-\frac{\mathcal{L}(\mathbf{C})}{\mathcal{L}_0}\right) \quad (18)$$

where $\mathcal{L}(\mathbf{C})$ is the loss function which depends both on data and parameters \mathbf{C} , and $\mathcal{L}_0 > 0$ is a *hyperparameter* associated with the likelihood function as opposed to a parameter in the parameterization. The posterior distribution, $\mathbb{P}(\mathbf{C}|\text{data})$, is then given by Bayes formula

$$\mathbb{P}(\mathbf{C}|\text{data}) \propto \mathbb{P}(\mathbf{C})\mathbb{P}(\text{data}|\mathbf{C}) \quad (19)$$

where $\mathbb{P}(\mathbf{C})$ is the prior distribution. In terms of probability densities, letting $\mathbb{P}(\mathbf{C}) \propto \rho^0(\mathbf{C})$ and $\mathbb{P}(\mathbf{C}|\text{data}) \propto \rho(\mathbf{C})$ denote our prior and posterior distributions for the parameters² \mathbf{C} , Bayes formula becomes

$$\rho(\mathbf{C}) \propto \rho^0(\mathbf{C}) \exp\left(-\frac{\mathcal{L}(\mathbf{C})}{\mathcal{L}_0}\right). \quad (20)$$

209 In our context Bayes' formula updates prior guesses about KPP parameter values and
210 yields a posterior distribution based on the LES data.

We choose the hyperparameter \mathcal{L}_0 as the minimum of the loss function $\mathcal{L}(\mathbf{C})$. The minimum is found using a modified simulated annealing procedure³ (Kirkpatrick et al., 1983). Once the parameter values \mathbf{C}^* that minimize the loss functions have been found, i.e. $\mathcal{L}_0 = \mathcal{L}(\mathbf{C}^*)$, the likelihood of any other parameter choice \mathbf{C}^1 is given by,

$$\rho(\mathbf{C}^1)/\rho(\mathbf{C}^*) = \exp\left(\frac{\mathcal{L}_0 - \mathcal{L}(\mathbf{C}^1)}{\mathcal{L}_0}\right). \quad (21)$$

211 For example, if the choice \mathbf{C}^1 increases the minimum of the loss function by a factor of
212 two, i.e. $\mathcal{L}(\mathbf{C}^1) = 2\mathcal{L}_0$, then it is $1/e$ less likely. The probability distribution $\rho(\mathbf{C})$ is
213 then sampled with a Random Walk Markov Chain Monte Carlo (RW-MCMC) algorithm
214 (Metropolis et al., 1953), described further in Appendix E.

215 To illustrate our choices, as well as the RW-MCMC algorithm, we show a typical
216 output from an RW-MCMC algorithm for a 2D probability distribution of the form in
217 equation 18. We use the probability density function for the KPP parameterization pre-
218 sented in the next section, but keep two of the four parameters fixed (C^D and C^H) to
219 reduce the problem from four to two parameters (C^N and C^S). The prior distributions
220 for C^N and C^S are uniform over the ranges reported at the end of this section. The pa-
221 rameters C^D and C^H are set to the values that minimize the loss function. We show re-
222 sults for two arbitrary values of \mathcal{L}_0 for illustrative purposes. Starting from a poor ini-
223 tial guess, the RW-MCMC search proceeds towards regions of higher probability (lower
224 loss function) by randomly choosing which direction to go. Once a region of high prob-
225 ability is found, in this case parameter values in the “blue” region, the parameters hover
226 around the minimum of the loss function as suggested by the high values of the likeli-
227 hood function. The orange hexagons represent the process of randomly walking towards
228 the minimum of the loss function and correspond to the “burn-in” period. The burn-
229 in period is often thrown away when calculating statistics since it corresponds to an ini-
230 tial transient before the RW-MCMC settles around the minimum of the likelihood func-
231 tion. We see that the choice of \mathcal{L}_0 does not change the overall structure of the proba-
232 bility distribution but does affect how far from optimal parameters the random walk is
233 allowed to drift.

² The proportionality sign is introduced, because Bayes' formula applies to probabilities, while $\rho^0(\mathbf{C})$ is a probability density function.

³ In simulated annealing one finds the minimum of the loss function decreasing \mathcal{L}_0 to zero as one explores the parameter space through a random walk. Here we keep updating \mathcal{L}_0 to the new local minimum every time the random walk stumbles on a set of parameters, for which $\mathcal{L}(\mathbf{C}) < \mathcal{L}_0$.

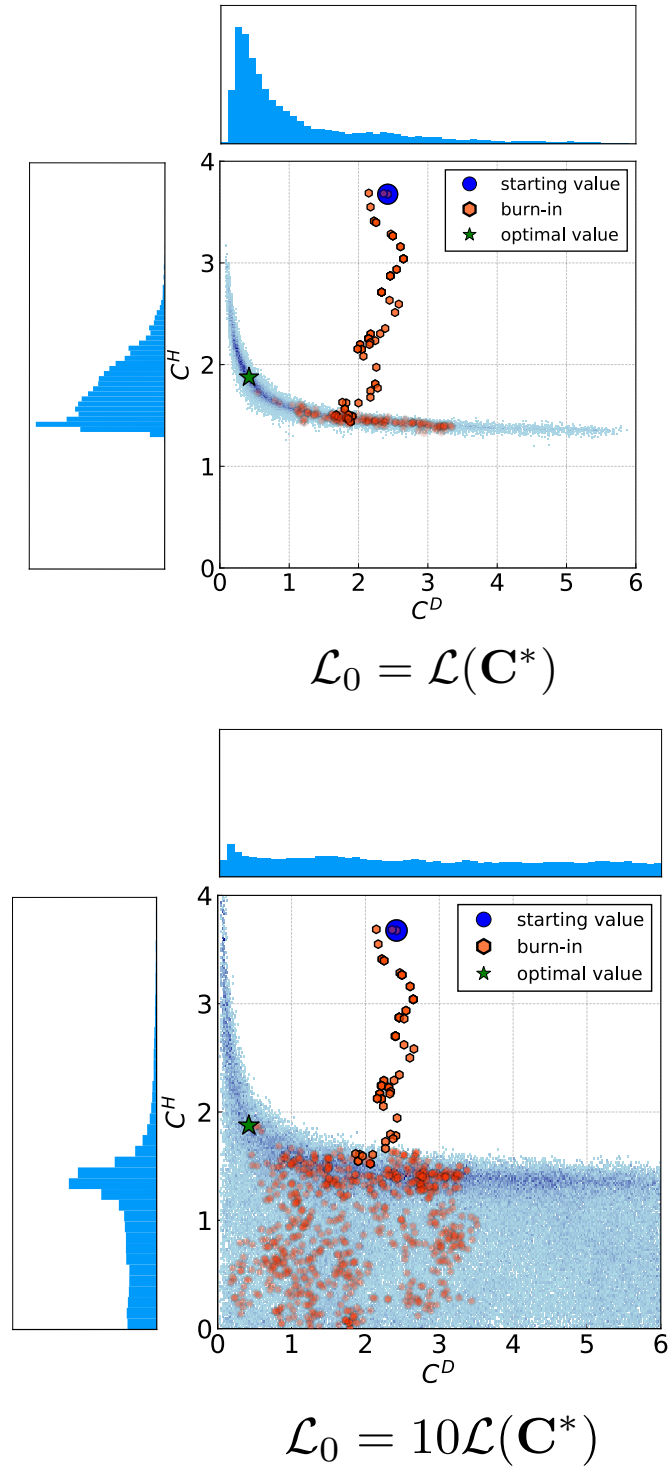


Figure 3. An example of a RW-MCMC search trajectory based on a sample probability distribution for KPP parameters using 10^5 RW-MCMC iterations. The trajectory starts from a region of very low probability (white areas) and moves toward progressively higher probabilities (the darker the blue shading, the higher the probability). The blue probability distributions on the left side and the top are the corresponding marginal distributions of C^H and C^D , respectively. The green star is the best known optimal of the probability distribution (i.e., the mode of the probability distribution). The value of $\mathcal{L}(\mathbf{C}^*)$ is the value of the loss function at the green star.

234 Parameterizations such as KPP exhibit a dependence on resolution in addition to
 235 nondimensional parameters. Here we perform all calculations for a vertical resolution
 236 $\Delta z = 6.25$ m and timestep $\Delta t = 10$ minutes representative of those used in state of
 237 the art ESMs. We do not use enhanced diffusivity as in (Large et al., 1994) for this res-
 238 olution. The parameterization is relatively insensitive to halving Δz and Δt , for a fixed
 239 set of parameters, but the results are sensitive to doubling either one. Thus the optimal
 240 parameter values and their uncertainties are only appropriate for the resolution used for
 241 the calibration and would need to be updated especially if the parameterization was run
 242 at a coarser resolution. This dependence on resolution could be handled within the Bayesian
 243 method by introducing Δz and Δt as additional parameters in the probability distribu-
 244 tion, but we do not pursue this approach.

The temporal window used to compute the loss function is from $t_1 = 0.25$ days
 (so as to eliminate initial transients in the LES) to the final simulation day chosen to
 be when $h \approx 70$ meters. We apply the Bayesian parameter estimation procedure to KPP
 using data from one LES simulation in section 3.1 and from multiple LES simulations
 using different initial stratifications in section 3.2. We use a uniform prior distributions
 for the KPP parameters over the following ranges:

$$0 \leq C^S \leq 1, \quad 0 \leq C^N \leq 8, \quad 0 \leq C^D \leq 6, \quad \text{and} \quad 0 \leq C^H \leq 5. \quad (22)$$

245 The surface layer fraction C^S , being a fraction, must stay between zero and one. The
 246 other parameter limits are chosen to span the whole range of physically plausible val-
 247 ues around the reference values given in equation (16). The choice of uniform distribu-
 248 tions is made to avoid favoring any particular value at the outset.

249 3.1 Calibration of KPP parameters from one LES simulation

250 In this section we apply the Bayesian calibration method to the LES simulation
 251 of penetrative convection described in section 2.1 and quantify uncertainties in KPP pa-
 252 rameters in section 2.2. The horizontal averages from the LES simulations are compared
 253 with predictions from solutions of the KPP boundary layer scheme, equations 9 and 10.
 254 The boundary and initial conditions for KPP are taken to be the same as those for the
 255 LES simulation, i.e., 100 W/m^2 cooling at the top, $\partial_z T = 0.01^\circ\text{C m}^{-1}$ at the bottom,
 256 and an initial profile $T_p(z, 0) = 20^\circ\text{C} + 0.01^\circ\text{C m}^{-1}z$.

257 To estimate the full probability distribution function, we use the RW-MCMC al-
 258 gorithm with 10^6 iterations to sample the probability distributions of the four KPP pa-
 259 rameters (C^S, C^N, C^D, C^H). The large number of forward runs is possible because the
 260 forward model consists of a one-dimensional equation, namely, KPP in single column mode.
 261 The Markov chain leads to roughly 10^4 statistically independent samples as estimated
 262 using an autocorrelation length, see Sokal (1997). The RW-MCMC algorithm generates
 263 the entire four dimensional PDF, equation 18.

264 The parameter probability distribution can be used to choose an optimal set of KPP
 265 parameters. Of the many choices, we pick the most probable value of the four dimen-
 266 sional probability distribution, the mode, because it minimizes the loss function, see Ap-
 267 pendix D for the detailed calculation. In figure 4a we show the horizontally averaged tem-
 268 perature profile from the LES simulation (continuous line) and the temperature profiles
 269 obtained running the KPP parameterization with reference and optimal parameters (squares
 270 and dots) at $t = 8$ days. The optimized temperature profiles are more similar to the
 271 LES simulation than the reference profiles especially in the entrainment region. Figure
 272 4b confirms that the square root of the instantaneous loss function, the error, grows much
 273 faster with the reference parameters. The oscillations in the error are a consequence of
 274 the coarseness of the KPP model: only one grid point is being entrained at any given
 275 moment.

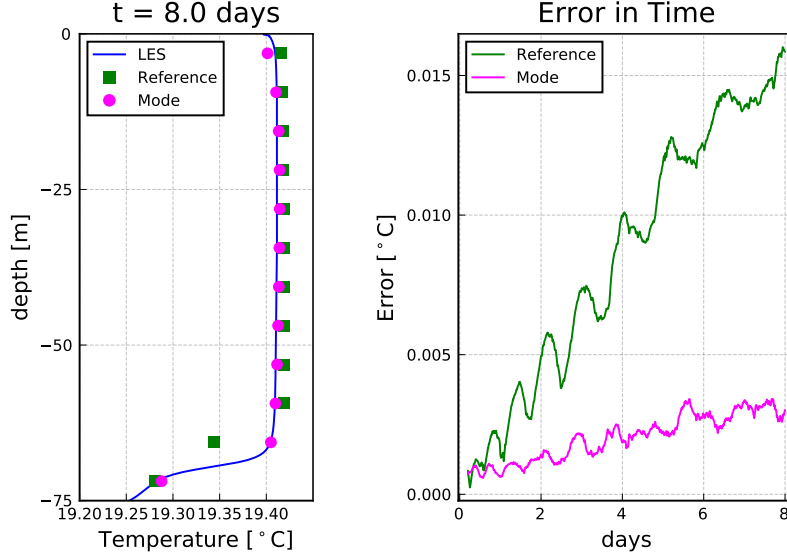


Figure 4. KPP and horizontally averaged LES temperature profiles for different point estimates of parameters at $t=8$ days as well as the error in time. In the left plot, the blue squares correspond to reference parameter choices, the red circles correspond to the optimized parameterization (using the mode of the probability distribution), and the blue line to the horizontally averaged LES solution, all at time $t=8$ days. On the right plot we show the instantaneous error at each moment in time. We see that the “optimal” parameter does indeed reduce the bias over the time period. The loss function is the largest square of the error over the time interval.

276 The improvement in boundary layer depth through optimization of the param-
 277 eters is about 10%, or 10 m over 8 days. As discussed in section 2.1, the rate of deep-
 278 ening can be predicted analytically within 20% by simply integrating the buoyancy bud-
 279 get over time and depth and assuming that the boundary layer is well mixed everywhere,
 280 i.e. ignoring the development of enhanced stratification within an entrainment layer at
 281 the base of the mixed layer. KPP improves on this prediction by including a param-
 282 eterization for the entrainment layer. The reference KPP parameters contribute a 10%
 283 improvement on the no entrainment layer prediction, and the optimized parameters con-
 284 tribute another 10%. While these may seem like modest improvements, they can pre-
 285 vent large biases for the boundary layer depth when integrated over a few months of cool-
 286 ing in winter rather than just 8 days. We will return to this point in the next section when
 287 we discuss structural deficiencies in the KPP formulation.

To visualize the probability distribution we focus on 2D marginal distributions, e.g.,

$$\rho_{2DM}(C^H, C^S) = \int \int \rho(\mathbf{C}) dC^D dC^N, \quad (23)$$

along with the other five possible pairings, as well as the 1D marginal distributions such as

$$\rho_M(C^H) \equiv \iiint \rho(\mathbf{C}) dC^S dC^D dC^N, \quad (24)$$

288 and similarly for the other three parameters.

289 The marginal distribution can intuitively be thought of as the total of a param-
 290 eter (or pair of parameters) while taking into account the total uncertainty of other pa-

291 parameters. Furthermore, the marginal distribution takes into account potential compen-
 292 sating effects that different parameters may have on one another. The marginal distri-
 293 bution does *not* capture the effect of individually varying a parameter while keeping all
 294 the other parameters fixed at a particular value⁴. That is an effect represented by a con-
 295 ditional distribution.

296 Constructing the marginal distributions only requires constructing histograms of
 297 the trajectories generated by the RW-MCMC algorithm. The 2D marginal distributions
 298 are visualized with heatmaps in figure 5 and the 1D marginal distributions of the cor-
 299 responding parameters are shown along the outermost edges. For the 2D marginal dis-
 300 tributions, the dark blue regions correspond to regions of high probability and the light
 301 blue regions are regions of low probability. The white space corresponds to regions that
 302 the RW-MCMC algorithm never visited. The 2D marginal distributions show that pa-
 303 rameters must be changed in tandem with one another in order to correspond to a sim-
 304 ilar model output. Furthermore their structure is distinctly non-Gaussian.

305 The 1D marginal distribution of the mixing depth parameter C^H (the bottom left
 306 rectangular panel) is much more compact than that of the other three parameters sug-
 307 gesting that it is the most sensitive parameter. The mixing depth parameter’s impor-
 308 tance stems from its control over both the buoyancy jump across the entrainment layer
 309 and the rate-of-deepening of the boundary layer. (Again it may be useful to remember
 310 that C^H is often referred to as the bulk Richardson number in the KPP literature, even
 311 though it takes a different meaning in convective simulations, see Appendix C.) The pa-
 312 rameters C^D and C^N set the magnitude of the local and nonlocal fluxes. Results are not
 313 sensitive to their specific values, as long as they are large enough to maintain a well-mixed
 314 layer. The value of the surface layer fraction C^S is peaked at lower values but is less sen-
 315 sitive to variations than C^D or C^H .

316 The uncertainties of the parameters can be used to infer the uncertainties of the
 317 temperature profile at each depth and time, predicted by KPP. To do this, we subsam-
 318 ple the 10^6 parameter values down to 10^4 and evolve KPP forward in time for each set
 319 of parameter choices. We construct histograms for the temperature field at the final time
 320 for each location in space individually. We then stack these histograms to create a vi-
 321 sual representation of the model uncertainty. This uncertainty quantifies the sensitiv-
 322 ity of the parameterization with respect to parameter perturbations as defined by the
 323 parameter distributions.

324 The histogram of temperature profiles at time $t = 8$ days as calculated by both
 325 our prior distribution (uniform distribution) and the posterior distribution (as obtained
 326 from the RW-MCMC algorithm) is visualized in figure 6. We see that there is a reduc-
 327 tion of the uncertainty in the temperature profile upon taking into account information
 328 gained from the LES simulation. The salient features of the posterior distribution tem-
 329 perature uncertainty are

- 330 1. 0-10 meter depth: There is some uncertainty associated with the vertical profile
 331 of temperature close to the surface.
- 332 2. 20-60 meter depth: The mean profile of temperature in the mixed layer is very well
 333 predicted by KPP.
- 334 3. 60-70 meter depth: The entrainment region contains the largest uncertainties.
- 335 4. 70-100 meter depth: There is virtually no uncertainty. The unstratified region be-
 336 low the boundary layer does not change from its initial value.

⁴That is, unless the other parameters have essentially delta function 1D marginal distributions.

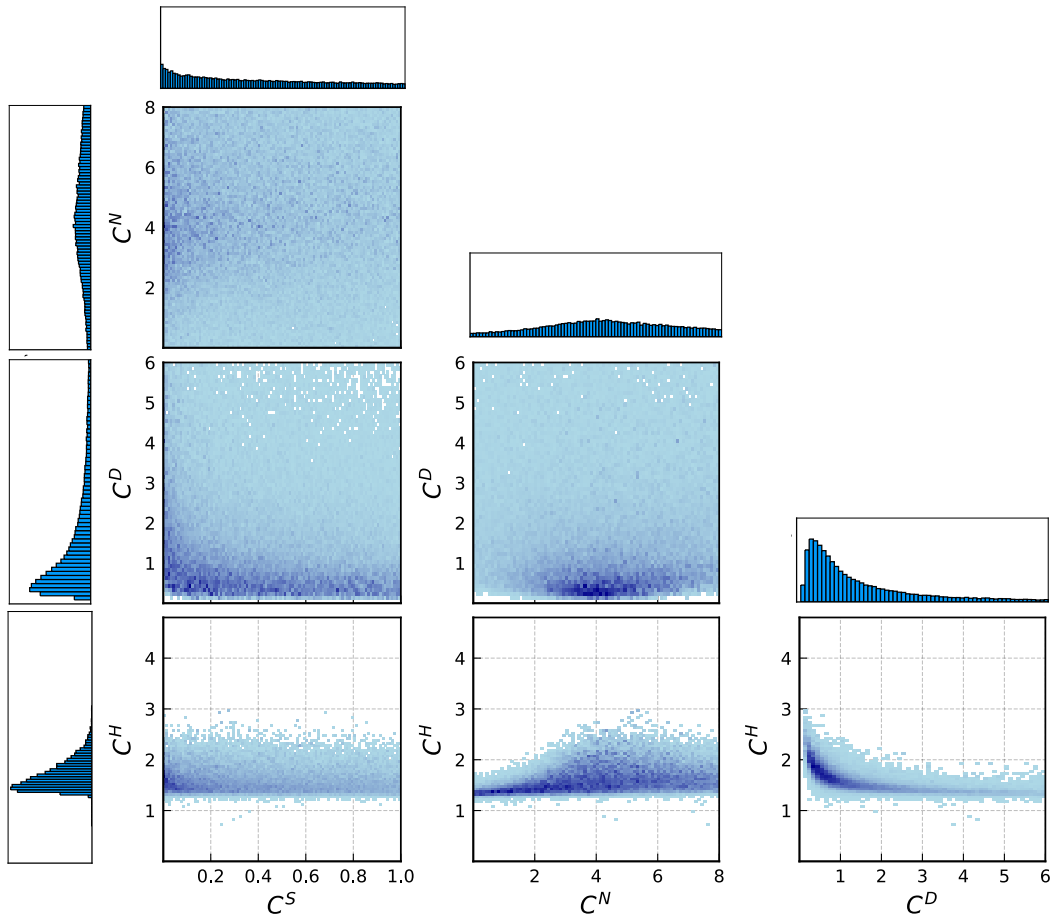


Figure 5. Marginal Distributions for KPP Parameters. The dark blue regions correspond to regions of high probability and the light blue regions are regions of low probability. The white space corresponds to regions that the RW-MCMC algorithm never visited. The corresponding 1D marginal distributions (corresponding to integrals of the 2D marginal distributions) are displayed on the left and on top of the plots for reference.

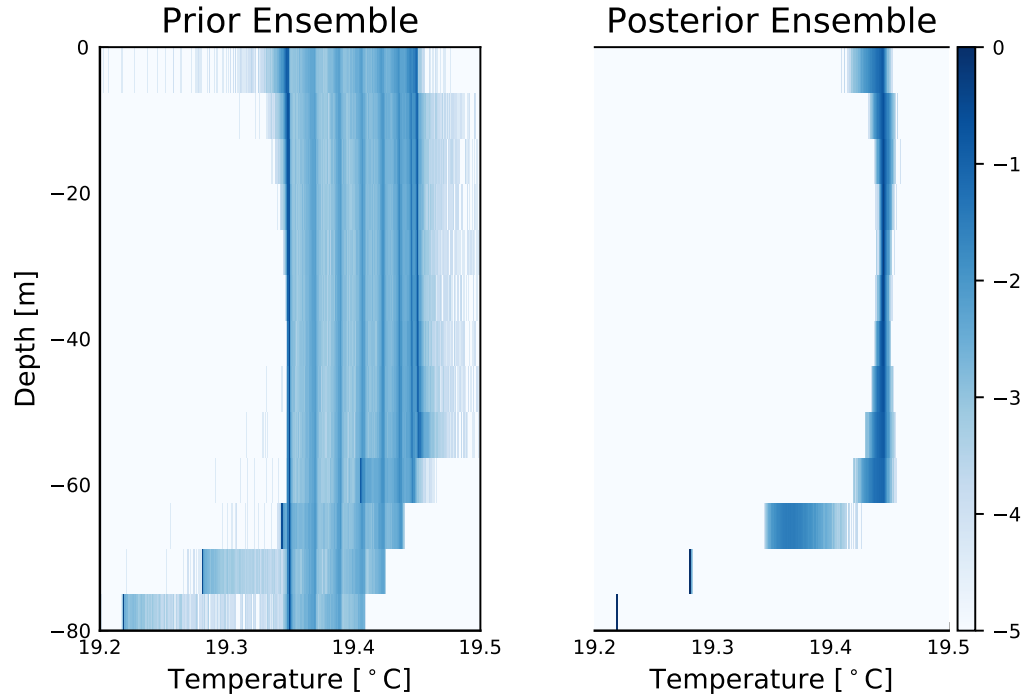


Figure 6. Uncertainty propagation of the temperature profile with respect to the prior and posterior probability distributions. The use of probability distributions for parameters has the consequence that the temperature field is no longer a point estimate, but rather a probability distribution at each moment in space and time. By sampling from the parameter probability distributions and evolving the parameterization forward in time, we obtain a succinct representation of what it means to “fiddle” with parameters. The legend on the right shows what the colors correspond to in terms of the base 10 logarithm of the probability distributions.

337 Now that we have applied the Bayesian methodology to one LES simulation and
 338 explored its implications, we are ready to apply the method to multiple LES simulations
 339 covering different regimes in the following section.

340 3.2 Calibration of KPP parameters from multiple LES simulations

341 We now use our Bayesian framework to explore possible sources of bias in the KPP
 342 model. To this end we investigate what happens when we change the initial stratifica-
 343 tion in penetrative convection simulations. This is motivated by recent work on bound-
 344 ary layer depth biases in the Southern Ocean (DuVivier et al., 2018; Large et al., 2019).
 345 In those studies, KPP failed to simulate deep boundary layers in winter when the sub-
 346 surface summer stratification was strong.

347 We perform 32 large eddy simulations and calculate parameter distributions for each
 348 case. In the previous section we saw that C^H is the most sensitive parameter. Thus our
 349 focus now will be on the optimization and uncertainty quantification of C^H . In the back-
 350 ground, however, we are estimating *all* parameters. We keep the surface cooling constant
 351 at 100 W/m^2 for all regimes, and only vary the initial stratification. The integration time
 352 was stopped when the boundary layer depth filled about 70% of the domain in each sim-
 353 ulation. We used 128^3 grid points in the LES, ≈ 0.8 meter resolution in each direction⁵.
 354 We use a lower resolution for the LES in these trend studies as compared to those in the
 355 previous section, but results were not sensitive to this change. In the Bayesian inference,
 356 each one of the probability distributions were calculated 10^5 iterations of RW-MCMC,
 357 leading to an effective sample size on the order of 10^3 . The stratifications ranged from
 358 $N^2 \approx 1 \times 10^{-6}$ to $N^2 \approx 3.3 \times 10^{-5} \text{ s}^{-2}$.

359 We find, as visualized in figure 7, that C^H is not constant but depends on the back-
 360 ground stratification, N^2 . The blue dots are the median values of the probability dis-
 361 tributions and the stars are the modes (minimum of the loss function). The error bars
 362 correspond to 90% probability intervals, meaning that 90% of parameter values fall be-
 363 tween the error bars. The large discrepancy between the median and the mode is due
 364 to the mode being the optimal value of the entire four dimensional distribution whereas
 365 the median only corresponds to the marginal distribution. The reference KPP value is
 366 plotted as a dashed line.

367 The median values and optimal values increase monotonically with the initial strat-
 368 ification revealing a systematic bias. Furthermore, it exposes *where* the systematic bias
 369 comes from: no single value of C^H , equation 15, can correctly reproduce the deepening
 370 of the boundary layer for all initial stratifications. This suggests that the scaling law for
 371 the boundary layer depth criteria is incommensurate with the LES data.

The failure of equation 15 can be understood by going back to the buoyancy bud-
 get in equation 7. Using the KPP estimate for the buoyancy jump across the entrain-
 ment layer,

$$\Delta b \equiv \frac{1}{C^S h} \int_{-C^S h}^0 B(z) dz - B(-h), \quad (25)$$

and introducing $N_h^2 \equiv \partial_z B(-h)$ for the stratification at the base of the entrainment
 layer to distinguish it from the interior stratification N^2 , we find that the boundary layer
 depth criterion, equation 15, implies,

$$h \Delta b \simeq C^H h^{4/3} (Q_b)^{1/3} N_h. \quad (26)$$

⁵ Although the parameter estimates will vary upon using less LES resolution, the qualitative trends are expected to be robust.

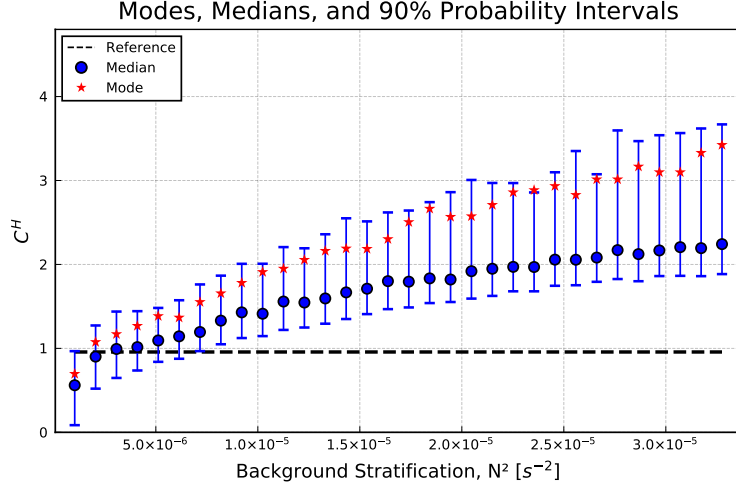


Figure 7. Mixing depth parameter optimized across various background stratification. The dots are the median values, the stars are the mode, and the error bars correspond to 90% probability intervals. The horizontal dashed line is the default value of the mixing depth parameter for reference. Here one can see that the mixing depth parameter when estimated across various regimes produces different results. This is a signature of a systematic bias in the parameterization.

Substituting this expression in the buoyancy budget, equation 7, one obtains an implicit equation for the evolution of the boundary layer depth h ,

$$\left(\frac{1}{2}N^2 - C^H (Q_b)^{1/3} h^{-2/3} N_h\right) h^2 \simeq Q_b t. \quad (27)$$

372 The LES simulation described in section 2.1, and many previous studies of penetrative
 373 convection, e.g. (Van Roekel et al., 2018; Deardorff et al., 1980), show that the bound-
 374 ary layer depth grows as \sqrt{t} . To be consistent, N_h would have to scale as $h^{2/3}$, but this
 375 is not observed in the LES simulations nor supported by theory. This suggests that we
 376 must modify the formulation of boundary layer depth, as we now describe.

377 3.3 Modification of the KPP parameterization to reduce biases

From the multi-regime study of the previous section we found that there is no optimal KPP mixing depth parameter C^H that works for arbitrary initial stratification. This prompted us to look for an alternative formulation of the depth criterion which satisfies the well known empirical result that the boundary layer depth deepens at a rate,

$$h \simeq \sqrt{c \frac{Q_b}{N^2} t}, \quad (28)$$

where c is a dimensionless constant found to be close to 3.0 with the LES simulation in section 2.1. Furthermore, c was found to be close to 3.0 across all the numerical experiments from section 3.2. Substituting this expression into the buoyancy budget, equation 7, we find that,

$$\frac{\Delta b}{h N^2} \simeq \left(\frac{1}{2} - \frac{1}{c}\right). \quad (29)$$

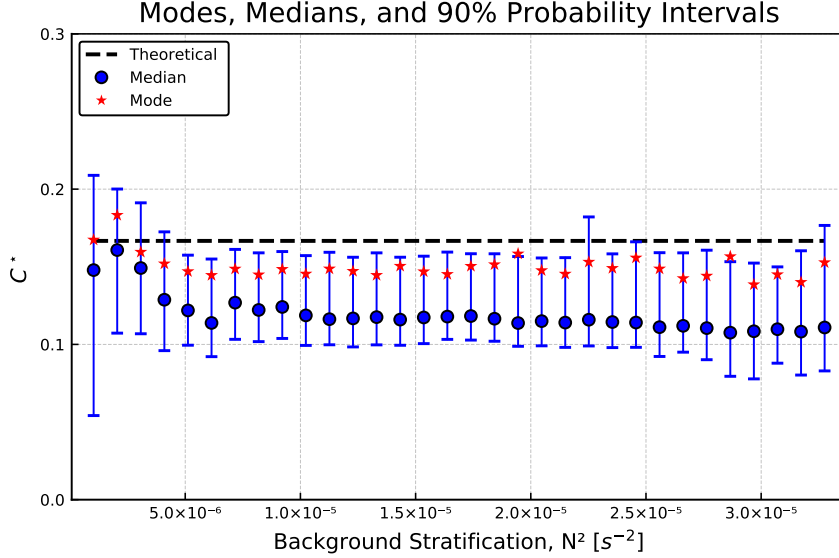


Figure 8. The modified mixing depth parameter optimized across various background stratification. The dots are the median values, the stars are the mode, and the error bars correspond to 90% probability intervals. The dashed line corresponds to $1/6$, the theoretical expectation based on equation 31. This is similar to figure 7, but using the modification from section 3.3. Here one can see that there mixing depth parameter when estimated across various regimes produces similar results. This is a desirable feature in a parameterization.

This expression can then be used as a new boundary layer depth criterion to replace equation 15,

$$C^* = \frac{h \left(\frac{1}{\bar{c}^s h} \int_{-C^s h}^0 B(z) dz - B(-h) \right)}{N^2 h^2 + 10^{-11} \text{m}^2 \text{s}^{-2}}, \quad (30)$$

where C^* replaces C^H as the dimensionless parameter whose value sets the boundary layer depth. The value of N^2 here is the background stratification. Based on equation 29 and our LES data, we expect

$$C^* \simeq \left(\frac{1}{2} - \frac{1}{c} \right) \simeq \frac{1}{6}. \quad (31)$$

378 Equation 30 is an implicit equation for h which guarantees that equation 28 holds.

379 We now repeat the model calibration in section 3.2 but using this new boundary
 380 layer depth criterion to test whether there is an optimal value of C^* that is independent
 381 of initial stratification. We estimate all KPP parameters and show the new mixing depth
 382 parameter for simulations with different initial stratifications in figure 8. Encouragingly
 383 there is no obvious trend in the optimal values of C^* and the error bars overlap for all
 384 cases. This supports the new criterion in the sense that parameters estimated in differ-
 385 ent regimes are now consistent with one another. The uncertainties in C^* translate into
 386 an uncertainty in boundary layer depth prediction. In particular, values between $0.05 \leq$
 387 $C^* \leq 0.2$ imply a boundary layer depth growth in the range $\sqrt{2.22tQ_b/N^2} \leq h \leq$
 388 $\sqrt{3.33tQ_b/N^2}$.

389 Additionally, one can check if the constants estimated following the methodology
 390 of section 3 are consistent with an *independent* measure directly from the diagnosed LES

391 simulation. In particular the LES simulations suggest that $C^* \simeq 1/6$ as per equation
 392 31. From figure 8 we see that the optimal C^* is smaller than $1/6 = 0.167$ (the dashed
 393 black line) and the value $1/6$ is not within the confidence intervals for many of the sim-
 394 ulations. There are several potential reasons for the discrepancy, e.g., the neglect of cur-
 395 vature in the buoyancy budget (since we assumed a piece-wise linear buoyancy profile)
 396 or the finite resolution of the parameterization. Perhaps the most likely explanation is
 397 the difference in how the boundary layer depth was diagnosed in the LES, which need
 398 not have the same meaning as the one in KPP. A different definition in the LES simu-
 399 lation, such as the depth of maximum stratification, would yield a different scaling law,
 400 but still proportional to \sqrt{t} . Whatever the choice, the Bayesian parameter estimation
 401 bypasses these ambiguities/inconsistencies by direct comparison with the entire horizon-
 402 tally average temperature profile from the LES.

403 We do not explore other modifications to the boundary layer depth criterion as this
 404 would greatly expand the scope of this article. Furthermore, biases in KPP are not lim-
 405 ited to the cases explored here, see Van Roekel et al. (2018) for discussions and reme-
 406 dies. The criterion described in this section assumes a constant initial stratification and
 407 a constant surface heat loss, which leads to the \sqrt{t} growth of the boundary layer depth.
 408 It would be interesting to extend the criterion to arbitrary initial stratification, variable
 409 surface heat fluxes, not to mention the interaction with wind-driven mixing. The goal
 410 here is not to derive a new parameterization, but rather to illustrate and argue for a Bayesian
 411 methodology in the refinement and assessment of parameterizations.

412 4 Discussion

413 We presented a Bayesian approach to assess the skill of the K-Profile Parameter-
 414 ization (KPP) for turbulent convection triggered by surface cooling in an initially sta-
 415 bly stratified ocean. The KPP model for this physical setting consists of a one dimen-
 416 sional model with an algebraic constraint for the mixing-layer depth together with four
 417 non-dimensional parameters. These parameters consisted of an algebraic reorganization
 418 of the original KPP parameters so that terms in the equations could be associated with
 419 choices of parameters. Parameters were estimated by reducing the mismatch between
 420 the vertical buoyancy profile predicted by KPP and the area-averaged buoyancy profile
 421 simulated with a three dimensional LES code for the same initial conditions and surface
 422 forcing. Using Bayes' formula we further estimated the full joint probability distribu-
 423 tion of the four parameters. Furthermore, the probability distribution was used to quan-
 424 tify inter-dependencies among parameters and their uncertainty around the optimal val-
 425 ues.

426 Repeating the Bayesian parameter optimization and uncertainty quantification for
 427 different initial stratifications, we found that no unique set of parameters could capture
 428 the deepening of convection in all cases. This implied that the KPP formulation does
 429 not capture the dependence of convection on the initial stratification in the simple test
 430 case considered here: constant surface cooling, constant initial stratification, no wind,
 431 and no background flow. The parameter that required re-tuning for each case was the
 432 one associated with the boundary layer depth criterion, thereby suggesting that this cri-
 433 terion has the wrong functional dependence on stratification. We thus reformulated the
 434 boundary layer depth criterion to capture the semi-analytical result, supported by the
 435 LES simulations, that the boundary layer depth deepens as the square root of time when
 436 the initial stratification is constant. The validity of the new formulation was vindicated
 437 because the Bayesian approach was able to find a set of parameters which captured the
 438 evolution of the boundary layer, as compared to the LES simulations, for all initial strat-
 439 ifications. In this way, the Bayesian methodology allowed us identify and remove a
 440 bias in KPP formulation.

441 The methodology outlined here could be as easily applied to other parameteriza-
 442 tions of boundary layer turbulence, such as those reviewed in CVMix (Griffies et al., 2015),
 443 Pacanowski and Philander (1981), Mellor and Yamada (1982), Price et al. (1986), and
 444 Kantha and Clayson (1994) . It is expected that the inclusion of additional physics, such
 445 as wind-driven mixing and its interaction with convection, would also be amenable to
 446 the techniques described in this manuscript. Our experience is that progress is faster if
 447 one starts with simple idealized setups, like the ones considered here, and then move to
 448 progressively more realistic ones which accounted for variable stratification and surface
 449 heat fluxes, wind-stress forcing, background shear, surface waves, etcetera. The Bayesian
 450 method would then provide a rigorous evaluation of parameter uncertainty, parameter
 451 dependencies, and biases in the formulation of the parameterization.

452 Ultimately, our hope is that parameter probability distributions estimated in lo-
 453 cal regimes will serve as useful prior information for calibration/tuning of Earth System
 454 Models (ESMs). Local simulations of turbulence must be carefully designed and incor-
 455 porate suites of subgrid-scale processes that have leading order impact in global ocean
 456 dynamics: surface and bottom boundary layer turbulence, surface wave effects, deep con-
 457 vection, mesoscale and submesoscale turbulence, and so forth. Bayesian calibration of
 458 parameterization for each subgrid-scale process will then result in probability distribu-
 459 tions for all the nondimensional parameters associated with the parameterizations. These
 460 distributions can then be used as prior information for what is a reasonable range of val-
 461 ues that each parameter can take, when the parameterizations are implemented in an
 462 ESMs.

463 With regards to calibration of ESMs, the parameterizations of different subgrid-
 464 scale processes may nonlinearly interact with each other and with the resolved physics.
 465 Additional calibration is then required for the full ESM. Presently this is achieved by
 466 perturbing the parameters within plausible ranges (Mauritsen et al., 2012; Schmidt et
 467 al., 2017). The Bayesian approach provides an objective approach to determine a plau-
 468 sible range. The same algorithm cannot be used to calibrate the ESM, because the method-
 469 ologies described here are not computationally feasible when applied to larger systems.
 470 Promising approaches to address this challenge through the use of surrogate models are
 471 described in Sraj et al. (2016) and Urrego-Blanco et al. (2016). Such models bring in-
 472 ternal sources of uncertainty and it is not clear to what extent one can trust a surrogate
 473 of a full ESM. One potential way to address this additional challenge is the Calibrate,
 474 Emulate, and Sample (CES) approach outlined in Cleary et al. (2020). There the sur-
 475 rogate model’s uncertainty is estimated through the use of Gaussian processes and in-
 476 cluded as part of a consistent Bayesian calibration procedure.

477 Should the global problem still exhibit significant biases, even when all available
 478 prior information about parameterizations and about global data are leveraged utiliz-
 479 ing emulators or traditional methods of tuning, then one would have to conclude that
 480 there is a fundamental deficiency in our understanding of how the different components
 481 of the climate system interact with one another, or that perhaps the models do not in-
 482 clude some key process. For example, Rye et al. (2020) argue that glacial melt might be
 483 one such missing process which is not currently represented in ESMs. The advantage of
 484 the systematic calibration approach outlined here is that it allows us to quantify uncer-
 485 tainty in ESM projections and identify the sources of such uncertainty.

486 **Appendix A Oceananigans.jl**

Oceananigans.jl (Ramadhan et al., 2020) is open source software for ocean process
 studies written in the Julia programming language (Bezanson et al., 2017; Besard et al.,
 2019). For the large eddy simulations (LESs) reported in this paper, Oceananigans.jl
 is configured to solve the spatially-filtered, incompressible Boussinesq equations with a tem-
 perature tracer. Letting $\mathbf{u} = (u, v, w)$ be the three-dimensional, spatially-filtered ve-

locity field, θ be the conservative temperature, p be the kinematic pressure, f be the Coriolis parameter, and $\boldsymbol{\tau}$ and \mathbf{q} be the stress tensor and temperature flux due to subfilter turbulent diffusion, the equations of motion are A1–A3,

$$\partial_t \mathbf{u} + (\mathbf{u} \cdot \nabla) \mathbf{u} + f \hat{z} \times \mathbf{u} + \nabla p = b \hat{z} - \nabla \cdot \boldsymbol{\tau}, \quad (\text{A1})$$

$$\partial_t \theta + \mathbf{u} \cdot \nabla \theta = -\nabla \cdot \mathbf{q}, \quad (\text{A2})$$

$$\nabla \cdot \mathbf{u} = 0. \quad (\text{A3})$$

The buoyancy b appearing in A1 is related to conservative temperature by a linear equation of state,

$$b = \alpha g (\theta_0 - \theta), \quad (\text{A4})$$

487 where $\theta_0 = 20^\circ \text{C}$ is a reference temperature, $\alpha = 2 \times 10^{-4} (\text{°C})^{-1}$ is the thermal ex-
 488 pansion coefficient, and $g = 9.81 \text{ m}^2 \text{ s}^{-1}$ is gravitational acceleration at the Earth’s sur-
 489 face.

490 A1 Subfilter stress and temperature flux

The subfilter stress and momentum fluxes are modeled with downgradient closures, such that

$$\tau_{ij} = -2\nu_e \Sigma_{ij} \quad \text{and} \quad \mathbf{q} = -\kappa_e \nabla \theta, \quad (\text{A5})$$

491 where $\Sigma_{ij} \equiv \frac{1}{2} (\partial_i u_j + \partial_j u_i)$ is the strain rate tensor, and ν_e and κ_e are the eddy vis-
 492 cosity and eddy diffusivity of conservative temperature. The eddy viscosity ν_e and eddy
 493 diffusivity κ_e in equation A5 are modeled with the anisotropic minimum dissipation (AMD)
 494 formalism introduced by (Rozema et al., 2015) and (Abkar et al., 2016), refined by (Verstappen,
 495 2018), and validated and described in detail for ocean-relevant scenarios by (Vreugdenhil
 496 & Taylor, 2018). AMD is simple to implement, accurate on anisotropic grids (Vreugdenhil
 497 & Taylor, 2018), and relatively insensitive to resolution (Abkar et al., 2016).

498 A2 Numerical methods

499 To solve equations A1–A3 with the subfilter model in equation A5 we use the soft-
 500 ware package ‘`Oceananigans.jl`’ written in the high-level Julia programming language
 501 to run on Graphics Processing Units, also called ‘GPUs’ (Bezanson et al., 2017; Besard
 502 et al., 2019; Besard et al., 2019). `Oceananigans.jl` uses a staggered C-grid finite vol-
 503 ume spatial discretization (Arakawa & Lamb, 1977) with centered second-order differ-
 504 ences to compute the advection and diffusion terms in equation A1 and equation A2, a
 505 pressure projection method to ensure the incompressibility of \mathbf{u} , a fast, Fourier-transform-
 506 based eigenfunction expansion of the discrete second-order Poisson operator to solve the
 507 discrete pressure Poisson equation on a regular grid (Schumann & Sweet, 1988), and second-
 508 order explicit Adams-Bashforth time-stepping. For more information about the staggered
 509 C-grid discretization and second-order Adams Bashforth time-stepping, see section 3 in
 510 (Marshall et al., 1997) and references therein. The code and documentation are avail-
 511 able for perusal at <https://github.com/ClimateMOC/Oceananigans.jl>.

512 Appendix B Parcel Theory Derivation for the KPP Boundary Layer 513 Depth Criterion

Here we summarise the derivation of the KPP boundary layer depth criterion for penetrative convection, because we could not find a succinct description in the published literature. Following (Deardorff et al., 1980) we consider the vertical momentum equation for a parcel punching through the entrainment layer,

$$w' \frac{dw'}{dz} \simeq -(b' - \bar{b}) \quad (\text{B1})$$

where b' is the buoyancy of the parcel, assumed to be equal to the mixed layer value, and \bar{b} is the area mean buoyancy profile in the entrainment layer. This equation holds if the area occupied by sinking plumes is small compared to the total area so that \bar{b} is a good proxy for the buoyancy in the environment around the plumes and $b' - \bar{b}$ represents the buoyancy force experienced by the parcel. The parcel velocity decelerates from $w' \equiv w_e$ at the mixed layer depth ($z = -h + \Delta h$) to zero at the boundary layer depth ($z = -h$) where turbulence vanishes. Assuming that the background stratification N_e^2 is approximately constant in the entrainment layer we also have $b' - \bar{b} = N_e^2(-h + \Delta h) - N_e^2 z$. The momentum equation can then be integrated from $z = -h + \Delta h$ to $z = -h$,

$$(w_e)^2 \simeq N_e^2 \Delta h^2, \quad (\text{B2})$$

assuming that the background stratification N_e^2 is constant in the entrainment layer. Introducing Δb as the difference between the environment buoyancy in the mixed layer and that at the base of the entrainment layer, we have $\Delta b = N_e^2 \Delta h$, and hence,

$$\Delta b \propto w^* N_e, \quad (\text{B3})$$

and (Deardorff et al., 1980) assumes that $w_e \propto w^*(-h + \Delta h)$. The criterion for diagnosing the boundary layer depth follows from this relationship; h is defined as the first depth z below the ocean surface where,

$$\frac{\Delta b(-h)}{w^*(-h)N_e(-h)} = C^H, \quad (\text{B4})$$

514 for some universal constant C^H . In the main text we show this scaling fails to predict
 515 the rate of deepening of the boundary layer depth in LES simulations. Further analy-
 516 sis, not reported here, show that this failure stems from relationship (B3) which is not
 517 supported by the simulations.

Equation (B4) is often referred to as a critical Richardson number criterion which may seem odd given that no Richardson number appears in the expression. This is best understood if one extends the criterion to the case when there is a momentum shear in the boundary layer, typically induced by mechanical stresses, such that in addition to a density jump $\Delta b(z)$ there is also a momentum jump $\Delta u(z)$ across the entrainment layer. The entrainment layer base is then found where the Richardson number matches a critical value Ri_c ,

$$Ri_c = \frac{\Delta b(-h)}{(\Delta u(-h))^2 + \frac{C^H}{Ri_c} w^*(-h)N_e(-h)}. \quad (\text{B5})$$

518 The rationale behind this extended criterion can be found in (Large et al., 1994). For
 519 the purely convective limit $\Delta u(-h) = 0$ and the dependence on Ri_c drops out.

520 **Appendix C Relationship between the model in section 2.2 and Large** 521 **et al. (1994)'s formulation of KPP**

522 The formulation of KPP in Section 2.2 represents an algebraic reorganization of
 523 the formulation proposed by Large et al. (1994). The two formulations are mathemat-
 524 ically equivalent. In this appendix, we discuss in detail how the four free parameters C^H ,
 525 C^S , C^D , and C^N are algebraically related to the free parameters proposed by Large et
 526 al. (1994).

527 Large et al. (1994)'s formulation of KPP for the case of penetrative convection with
 528 no horizontal shear introduces six nondimensional parameters: the Von Karman constant
 529 $\kappa = 0.4$, the ratio of the entrainment flux to the surface flux $\beta_T = 0.2$, a constant that
 530 sets the amplitude of the non-local flux $C^* = 10$, a constant that ensures the continu-
 531 ity of the buoyancy flux profile $c_s = 98.96$, the surface layer fraction $\epsilon = 0.1$, and a

532 parameter that controls the smoothing of the buoyancy profile at the base of the bound-
 533 ary layer depth C_v . Large et al. (1994) argue that C_v can take any value between 1 and
 534 2. We set the reference value $C_v = 1.7$, which corresponds to the strong stratification
 535 limit in the model proposed by Danabasoglu et al. (2006) and given by equation (8.184)
 536 in Griffies et al. (2015).

In our formulation we introduce four parameters which are related to the original
 Large et al. (1994) parameters as follows,

$$C^H = \frac{C_v(\beta_T)^{1/2}}{(c_s\kappa^4\epsilon)^{1/6}}, \quad C^S = \epsilon, \quad C^D = (c_s\kappa^4)^{1/3}, \quad \text{and} \quad C^N = C^*(c_s\kappa^4\epsilon)^{1/3}. \quad (\text{C1})$$

537 We are able to reduce the number of parameters from six ($\epsilon, c_s, C_v, \beta_T, \kappa, C^*$) to four
 538 (C^H, C^S, C^D, C^N), because in the case of penetrative convection the two combinations
 539 $C_v(\beta_T)^{1/2}$ and $c_s\kappa^4$ always appear together.

Using the reference KPP parameter values reported above, our parameters take the
 values:

$$C^H = 0.956, \quad C^S = 0.1, \quad C^D = 1.36, \quad C^N = 6.3275. \quad (\text{C2})$$

540 We refer to these as the reference parameters.

It is worth commenting why the critical Richardson number, the focus of much liter-
 ature on KPP, does not appear when considering penetrative convection. The bound-
 ary layer depth is determined implicitly through equations (21) and (23) in Large et al.
 (1994),

$$\text{Ri}_b(z) = \frac{(B_r - B(z))(-z)}{|V_r - V(z)|^2 + V_t^2(z)} \quad \text{and} \quad V_t^2(z) = \frac{C_v(\beta_T)^{1/2}}{\text{Ri}_c\kappa^2} (c_s\epsilon)^{-1/2} (-z)Nw_s, \quad (\text{C3})$$

where B is buoyancy and B_r is the average of B between the surface and the depth ϵz .
 The boundary layer depth is defined as the depth $z = -h$ where $\text{Ri}_b(-h) = \text{Ri}_c$. For
 convection without shear, the case considered in this paper, $|V_r - V(z)|^2 = 0$ and $w_s =$
 $w^*(c_s\epsilon)^{1/3}\kappa^{4/3}$. The two equations can therefore be combined together:

$$\frac{C_v(\beta_T)^{1/2}}{\kappa^{2/3}} (c_s\epsilon)^{-1/6} = \frac{(B_r - B(-h))h}{hNw^*}. \quad (\text{C4})$$

541 and the critical Richardson number drops out from the expression. This expression fur-
 542 ther supports our decision to introduce the single parameter C^H in favor of the combi-
 543 nation of original parameters appearing on the left hand side of (C4). In penetrative con-
 544 vection it is the parameter C^H that controls the boundary layer depth rather than the
 545 critical Richardson number.

The optimal parameters and probability distributions for (C^H, C^S, C^D, C^N) can
 be mapped onto ($\epsilon, C_v(\beta_T)^{1/2}, c_s\kappa^4, C^*$) using the inverse transformation,

$$\epsilon = C^S, \quad c_s\kappa^4 = (C^D)^3, \quad C^* = \frac{C^N}{C^D(C^S)^{1/3}}, \quad \text{and} \quad C_v(\beta_T)^{1/2} = C^H(C^D)^{1/2}(C^S)^{1/6}. \quad (\text{C5})$$

546 Appendix D A Primer on Uncertainty Quantification

547 The probability distribution of the parameters in a parameterization must quan-
 548 tify the likelihood that the parameters take on values other than those that minimize
 549 the loss function \mathcal{L} . To achieve this the probability distribution must satisfy two key prop-
 550 erties:

- 551 1. In the limit of no uncertainty, the probability distribution should collapse to a delta
 552 function centered at the optimal parameter values that minimize the loss function.

- 553 2. The uncertainty of a parameter value \mathbf{C} should increase proportionally to the value
554 of $\mathcal{L}(\mathbf{C})$.

There are many probability distributions that satisfy the above properties. We choose the following:

$$\rho(\mathbf{C}) \propto \rho^0(\mathbf{C}) \exp(-\mathcal{L}(\mathbf{C})/\mathcal{L}_0), \quad (\text{D1})$$

555 where ρ^0 is a uniform prior distribution, \mathcal{L} is a loss function, and \mathcal{L}_0 is a hyperparam-
556 eter.

557 The hyperparameter \mathcal{L}_0 sets the shape of the likelihood function $\exp(-\mathcal{L}(\mathbf{C})/\mathcal{L}_0)$
558 and its associated uncertainty quantification. The limit $\mathcal{L}_0 \rightarrow 0$ corresponds to no un-
559 certainty, because the likelihood function and the probability distribution collapse to a
560 delta function peaked at the optimal parameter values that minimize the loss function.
561 The limit $\mathcal{L}_0 \rightarrow \infty$ instead corresponds to a likelihood function that adds no informa-
562 tion to reduce the uncertainty and the posterior distribution $\rho(\mathbf{C})$ is equal to the prior
563 one $\rho_0(\mathbf{C})$. Thus \mathcal{L}_0 must take finite values between zero and infinity, if the likelihood
564 function is to add useful information.

For any finite value of \mathcal{L}_0 , the probability distribution has its mode (maximum)
at the optimal parameters, if the prior distribution is uniform. This can be easily demon-
strated. Let \mathbf{C}^* denote the parameter values for which the loss function has its global
minimum and \mathbf{C} denote any other set of parameter values. It is then the case that $\rho(\mathbf{C})$
is smaller than $\rho(\mathbf{C}^*)$ for any \mathbf{C} ,

$$\mathcal{L}(\mathbf{C}^*) \leq \mathcal{L}(\mathbf{C}) \Rightarrow \exp(-\mathcal{L}(\mathbf{C})/\mathcal{L}_0) \leq \exp(-\mathcal{L}(\mathbf{C}^*)/\mathcal{L}_0) \Rightarrow \rho(\mathbf{C}) \leq \rho(\mathbf{C}^*). \quad (\text{D2})$$

565 Hence the most probable value of the probability distribution is achieved at the mini-
566 mum of the loss function independent of \mathcal{L}_0 for a uniform prior distribution.

567 As mentioned in section 3, it is convenient to set the hyperparameter \mathcal{L}_0 to be equal
568 to the minimum of the loss function $\mathcal{L}(\mathbf{C}^*)$. This choice satisfies two key requirements.
569 First, the uncertainties of parameters should be independent of the units of the loss func-
570 tion. Second, the hyperparameter \mathcal{L}_0 should be larger the larger the loss function $\mathcal{L}(\mathbf{C}^*)$,
571 because the latter is a measure of the parameterization bias and the former should be
572 larger if there is more uncertainty about acceptable parameter values.

573 In practice it is seldom possible to find the global minimum of \mathcal{L} and instead we
574 adopt a “best guess” of the optimal parameters $\tilde{\mathbf{C}}$ and set $\tilde{\mathcal{L}}_0 = \mathcal{L}(\tilde{\mathbf{C}})$. Since $\mathcal{L}(\mathbf{C}^*) \leq$
575 $\mathcal{L}(\tilde{\mathbf{C}})$, our choice is conservative because a larger \mathcal{L}_0 corresponds to *more* uncertainty.

576 Appendix E Random Walk Markov Chain Monte Carlo

577 We use the Random Walk Markov Chain Monte Carlo Method (RW-MCMC) in-
578 troduced by Metropolis et al. (1953) to sample values from the probability distribution.
579 While other more efficient algorithms exist, our parameter space is only four dimensional
580 and computational cost is not an issue. The RW-MCMC samples the probability func-
581 tion by taking a random walk through parameter space. The algorithm generates a se-
582 quence of sample parameter values \mathbf{C}_i in such a way that, as more and more sample val-
583 ues are produced, the distribution of values more closely approximates the joint param-
584 eter probability distribution of the parameters. At each iteration, the algorithm picks
585 a candidate parameter set for the next sample value based on the current sample value.
586 Then, with some probability, the candidate parameter set is either accepted (in which
587 case the candidate value is used in the next iteration) or rejected (in which case the can-
588 didate value is discarded, and current values reused in the next iteration). The criterion
589 for acceptance and its relation to the probability distribution is best described by sketch-
590 ing the algorithm:

- 591 1. Choose a set of initial parameter values \mathbf{C}_0 . We pick our best guess at the set of
592 values that minimize the log-likelihood function as estimated from standard min-
593 imization techniques.
- 594 2. Choose a new set of candidate parameters by adding a Gaussian random variable
595 with mean zero and covariance matrix Σ to the initial set, $\tilde{\mathbf{C}}_1 = \mathbf{C}_0 + \mathcal{N}(0, \Sigma)$.
596 The algorithm is guaranteed to work *independently* of the choice of Σ as long as
597 it is nonzero and does not vary throughout the random walk. However suitable
598 choices can speed up convergence and will be discussed below.
- 599 3. Calculate $\Delta\ell = \ell(\mathbf{C}_0) - \ell(\tilde{\mathbf{C}}_1)$. This is a measure of how much more likely $\tilde{\mathbf{C}}_1$
600 is relative to \mathbf{C}_0 .
- 601 4. Draw a random variable from the interval $[0, 1]$, e.g. calculate $u = \mathcal{U}(0, 1)$. If $\log(u) <$
602 $\Delta\ell$ accept the new parameter values and set $\mathbf{C}_1 = \tilde{\mathbf{C}}_1$. Otherwise reject the new
603 parameter values $\mathbf{C}_1 = \mathbf{C}_0$. This is the “accept / reject” step. Note that if $\Delta\ell >$
604 0 , i.e. if the proposed parameter produces a smaller output in the negative log-
605 likelihood function, the proposal is always accepted.
- 606 5. Repeat steps 2-4, replacing $\mathbf{C}_0 \rightarrow \mathbf{C}_i$ and $\mathbf{C}_1 \rightarrow \mathbf{C}_{i+1}$, to generate a sequence
607 for \mathbf{C}_i of parameter values.

608 The sequence of parameter values generated by the algorithm can then be used to con-
609 struct any statistics of the probability distribution 18, including empirical distributions,
610 marginal distributions, and joint distributions. In the context of KPP it can generate
611 the uncertainty of the temperature value at any depth and time as well as the uncertainty
612 of the boundary layer depth at a given time.

613 To guide the choice of an appropriate value for Σ , one diagnoses the “number of
614 independent samples” by using approximations of the correlation length as described by
615 Sokal (1997). If Σ is too small then the acceptance rate is too large since each candidate
616 parameter is barely any different from the original one. Too large a Σ yields too low ac-
617 ceptance rates. To find an appropriate compromise we perform a preliminary random
618 walk and estimate the covariance matrix of the resulting distribution. We then set Σ equal
619 to this covariance matrix.

620 Last, in order to sample parameters within a finite domain, we artificially make the
621 parameter space periodic and the random walk is therefore guaranteed to never leave the
622 desired domain.

623 Acknowledgments

624 The authors would like to thank Carl Wunsch, Tapio Schneider, Andrew Stuart, and William
625 Large for numerous illuminating discussions. We would also like to thank the review-
626 ers for their helpful suggestions with the manuscript. Our work is supported by the gen-
627 erosity of Eric and Wendy Schmidt by recommendation of the Schmidt Futures program,
628 and by the National Science Foundation under grant AGS-6939393. Code and data may
629 be found via figshare at (Souza, 2020).

630 References

- 631 Abkar, M., Bae, H. J., & Moin, P. (2016). Minimum-dissipation scalar transport
632 model for large-eddy simulation of turbulent flows. *Physical Review Fluids*,
633 *1*(4), 041701. doi: 10.1103/PhysRevFluids.1.041701
- 634 Arakawa, A., & Lamb, V. R. (1977). Computational design of the basic dynamical
635 processes of the ucla general circulation model. In J. Chang (Ed.), *General*
636 *circulation models of the atmosphere* (Vol. 17, p. 173 - 265). Elsevier. doi: 10
637 .1016/B978-0-12-460817-7.50009-4
- 638 Bayes, T. (1763). An essay towards solving a problem in the doctrine of chances.
639 *Phil. Trans. of the Royal Soc. of London*, *53*, 370–418.

- 640 Besard, T., Churavy, V., Edelman, A., & Sutter, B. D. (2019). Rapid software pro-
 641 tototyping for heterogeneous and distributed platforms. *Advances in Engineering*
 642 *Software*, *132*, 29 - 46. Retrieved from [http://www.sciencedirect.com/](http://www.sciencedirect.com/science/article/pii/S0965997818310123)
 643 [science/article/pii/S0965997818310123](http://www.sciencedirect.com/science/article/pii/S0965997818310123) doi: [https://doi.org/10.1016/](https://doi.org/10.1016/j.advengsoft.2019.02.002)
 644 [j.advengsoft.2019.02.002](https://doi.org/10.1016/j.advengsoft.2019.02.002)
- 645 Besard, T., Foket, C., & De Sutter, B. (2019, April). Effective extensible pro-
 646 gramming: Unleashing julia on gpus. *IEEE Transactions on Parallel and*
 647 *Distributed Systems*, *30*(4), 827-841. doi: 10.1109/TPDS.2018.2872064
- 648 Bezanson, J., Edelman, A., Karpinski, S., & Shah, V. B. (2017). Julia: A Fresh
 649 Approach to Numerical Computing. *SIAM Review*, *59*(1), 65-98. doi: 10/
 650 f9wkpj
- 651 Cenedese, C., Marshall, J., & Whitehead, J. A. (2004, 03). A Laboratory Model of
 652 Thermocline Depth and Exchange Fluxes across Circumpolar Fronts*. *Journal*
 653 *of Physical Oceanography*, *34*(3), 656-667. Retrieved from [https://doi.org/](https://doi.org/10.1175/2508.1)
 654 [10.1175/2508.1](https://doi.org/10.1175/2508.1) doi: 10.1175/2508.1
- 655 Cleary, E., Garbuno-Inigo, A., Lan, S., Schneider, T., & Stuart, A. M. (2020). Cali-
 656 brate, emulate, sample. *arXiv:2001.03689 [stat.CO]*. Retrieved from [https://](https://arxiv.org/abs/2001.03689)
 657 arxiv.org/abs/2001.03689
- 658 Danabasoglu, G., Large, W. G., Tribbia, J. J., Gent, P. R., Briegleb, B. P., &
 659 McWilliams, J. C. (2006). Diurnal coupling in the tropical oceans of ccm3.
 660 *Journal of climate*, *19*(11), 2347-2365.
- 661 Deardorff, J. W., Willis, G. E., & Stockton, B. H. (1980). Laboratory studies of
 662 the entrainment zone of a convectively mixed layer. *Journal of Fluid Mechan-*
 663 *ics*, *100*(1), 41-64. doi: 10.1017/S0022112080001000
- 664 DuVivier, A. K., Large, W. G., & Small, R. J. (2018). Argo observations of
 665 the deep mixing band in the southern ocean: A salinity modeling chal-
 666 lenge. *Journal of Geophysical Research: Oceans*, *123*(10), 7599-7617. doi:
 667 [10.1029/2018JC014275](https://doi.org/10.1029/2018JC014275)
- 668 Frisch, U. (1995). *Turbulence: The legacy of a. n. kolmogorov*. Cambridge University
 669 Press. doi: 10.1017/CBO9781139170666
- 670 Griffies, S., Levy, M., Adcroft, A., Danabasoglu, G., Hallberg, R., Jacobsen, D., ...
 671 Ringler, T. (2015). *Theory and numerics of the community ocean vertical*
 672 *mixing (cvmix) project* (Draft from March 9, 2015).
- 673 Harcourt, R. R. (2015). An improved second-moment closure model of langmuir
 674 turbulence. *Journal of Physical Oceanography*, *45*(1), 84-103. Retrieved from
 675 <https://doi.org/10.1175/JPO-D-14-0046.1> doi: 10.1175/JPO-D-14-0046
 676 .1
- 677 Hourdin, F., Mauritsen, T., Gettelman, A., Golaz, J.-C., Balaji, V., Duan, Q.,
 678 ... Williamson, D. (2017). The art and science of climate model tun-
 679 ing. *Bulletin of the American Meteorological Society*, *98*(3), 589-602. doi:
 680 [10.1175/BAMS-D-15-00135.1](https://doi.org/10.1175/BAMS-D-15-00135.1)
- 681 Jaynes, E. T. (2003). *Probability theory: The logic of science* (G. L. Bretthorst,
 682 Ed.). Cambridge University Press. doi: 10.1017/CBO9780511790423
- 683 Kantha, L. H., & Clayson, C. A. (1994). An improved mixed layer model for geo-
 684 physical applications. *Journal of Geophysical Research: Oceans*, *99*(C12),
 685 25235-25266. Retrieved from [https://agupubs.onlinelibrary.wiley.com/](https://agupubs.onlinelibrary.wiley.com/doi/abs/10.1029/94JC02257)
 686 [doi/abs/10.1029/94JC02257](https://agupubs.onlinelibrary.wiley.com/doi/abs/10.1029/94JC02257) doi: 10.1029/94JC02257
- 687 Kirkpatrick, S., Gelatt, C. D., & Vecchi, M. P. (1983). Optimization by simulated
 688 annealing. *Science*, *220*(4598), 671-680. doi: 10.1126/science.220.4598.671
- 689 Large, W. G., McWilliams, J. C., & Doney, S. C. (1994). Oceanic vertical mixing: A
 690 review and a model with a nonlocal boundary layer parameterization. *Reviews*
 691 *of Geophysics*, *32*(4), 363-403. doi: 10.1029/94RG01872
- 692 Large, W. G., Patton, E. G., DuVivier, A. K., Sullivan, P. P., & Romero, L. (2019).
 693 Similarity theory in the surface layer of large-eddy simulations of the wind-,
 694 wave-, and buoyancy-forced southern ocean. *Journal of Physical Oceanography*,

- 695 49(8), 2165-2187. doi: 10.1175/JPO-D-18-0066.1
- 696 Li, Q., & Fox-Kemper, B. (2017). Assessing the effects of langmuir turbulence on
697 the entrainment buoyancy flux in the ocean surface boundary layer. *Journal of*
698 *Physical Oceanography*, 47(12), 2863-2886. Retrieved from [https://doi.org/](https://doi.org/10.1175/JPO-D-17-0085.1)
699 [10.1175/JPO-D-17-0085.1](https://doi.org/10.1175/JPO-D-17-0085.1) doi: 10.1175/JPO-D-17-0085.1
- 700 Marshall, J., Adcroft, A., Hill, C., Perelman, L., & Heisey, C. (1997). A finite-
701 volume, incompressible navier stokes model for studies of the ocean on parallel
702 computers. *Journal of Geophysical Research: Oceans*, 102(C3), 5753-5766. doi:
703 10.1029/96JC02775
- 704 Marshall, J., & Schott, F. (1999). Open-ocean convection: Observations, theory, and
705 models. *Reviews of Geophysics*, 37(1), 1-64. doi: 10.1029/98RG02739
- 706 Mauritsen, T., Stevens, B., Roeckner, E., Crueger, T., Esch, M., Giorgetta, M.,
707 ... Tomassini, L. (2012). Tuning the climate of a global model. *Journal*
708 *of Advances in Modeling Earth Systems*, 4(3). Retrieved from [https://](https://agupubs.onlinelibrary.wiley.com/doi/abs/10.1029/2012MS000154)
709 agupubs.onlinelibrary.wiley.com/doi/abs/10.1029/2012MS000154 doi:
710 10.1029/2012MS000154
- 711 Mellor, G. L., & Yamada, T. (1982). Development of a turbulence closure model for
712 geophysical fluid problems. *Reviews of Geophysics*, 20(4), 851-875. Retrieved
713 from [https://agupubs.onlinelibrary.wiley.com/doi/abs/10.1029/](https://agupubs.onlinelibrary.wiley.com/doi/abs/10.1029/RG020i004p00851)
714 [RG020i004p00851](https://agupubs.onlinelibrary.wiley.com/doi/abs/10.1029/RG020i004p00851) doi: 10.1029/RG020i004p00851
- 715 Metropolis, N., Rosenbluth, A. W., Rosenbluth, M. N., Teller, A. H., & Teller, E.
716 (1953). Equation of state calculations by fast computing machines. *The*
717 *Journal of Chemical Physics*, 21(6), 1087-1092. doi: 10.1063/1.1699114
- 718 Morrison, H., van Lier-Walqui, M., Kumjian, M. R., & Prat, O. P. (2020). A
719 bayesian approach for statistical-physical bulk parameterization of rain mi-
720 crophysics. part i: Scheme description. *Journal of the Atmospheric Sci-*
721 *ences*, 77(3), 1019-1041. Retrieved from [https://doi.org/10.1175/](https://doi.org/10.1175/JAS-D-19-0070.1)
722 [JAS-D-19-0070.1](https://doi.org/10.1175/JAS-D-19-0070.1) doi: 10.1175/JAS-D-19-0070.1
- 723 Nadiga, B., Jiang, C., & Livescu, D. (2019). Leveraging bayesian analysis to improve
724 accuracy of approximate models. *Journal of Computational Physics*, 394, 280 -
725 297. Retrieved from [http://www.sciencedirect.com/science/article/pii/](http://www.sciencedirect.com/science/article/pii/S0021999119303407)
726 [S0021999119303407](http://www.sciencedirect.com/science/article/pii/S0021999119303407) doi: <https://doi.org/10.1016/j.jcp.2019.05.015>
- 727 Pacanowski, R. C., & Philander, S. G. H. (1981, 11). Parameterization of
728 Vertical Mixing in Numerical Models of Tropical Oceans. *Journal of*
729 *Physical Oceanography*, 11(11), 1443-1451. Retrieved from [https://](https://doi.org/10.1175/1520-0485(1981)011<1443:POVMIN>2.0.CO;2)
730 [doi.org/10.1175/1520-0485\(1981\)011<1443:POVMIN>2.0.CO;2](https://doi.org/10.1175/1520-0485(1981)011<1443:POVMIN>2.0.CO;2) doi:
731 10.1175/1520-0485(1981)011<1443:POVMIN>2.0.CO;2
- 732 Price, J. F., Weller, R. A., & Pinkel, R. (1986, July). Diurnal cycling: Observations
733 and models of the upper ocean response to diurnal heating, cooling, and wind
734 mixing. , 91(C7), 8411-8427. doi: 10.1029/JC091iC07p08411
- 735 Ramadhan, A., Wagner, G. L., Hill, C., Campin, J.-M., Churavy, V., Besard, T.,
736 ... Marshall, J. (2020). Oceananigans.jl: Fast and friendly geophysical fluid
737 dynamics on GPUs. *Journal of Open Source Software*, 5(53), 2018. Retrieved
738 from <https://doi.org/10.21105/joss.02018> doi: 10.21105/joss.02018
- 739 Reichl, B. G., Wang, D., Hara, T., Ginis, I., & Kukulka, T. (2016). Langmuir tur-
740 bulence parameterization in tropical cyclone conditions. *Journal of Physical*
741 *Oceanography*, 46(3), 863-886. Retrieved from [https://doi.org/10.1175/](https://doi.org/10.1175/JPO-D-15-0106.1)
742 [JPO-D-15-0106.1](https://doi.org/10.1175/JPO-D-15-0106.1) doi: 10.1175/JPO-D-15-0106.1
- 743 Rozema, W., Bae, H. J., Moin, P., & Verstappen, R. (2015). Minimum-dissipation
744 models for large-eddy simulation. *Physics of Fluids*, 27(8), 085107. doi: 10
745 .1063/1.4928700
- 746 Rye, C. D., Marshall, J., Kelley, M., Russell, G., Nazarenko, L. S., Kostov, Y.,
747 ... Hansen, J. (2020). Antarctic glacial melt as a driver of recent south-
748 ern ocean climate trends. *Geophys. Res. Lett.*, 47(11), e2019GL086892. doi:
749 10.1029/2019GL086892

- 750 Schmidt, G. A., Bader, D., Donner, L. J., Elsaesser, G. S., Golaz, J.-C., Hannay, C.,
 751 ... Saha, S. (2017). Practice and philosophy of climate model tuning across
 752 six us modeling centers. *Geoscientific Model Development*, 10(9), 3207–3223.
 753 Retrieved from <https://gmd.copernicus.org/articles/10/3207/2017/>
 754 doi: 10.5194/gmd-10-3207-2017
- 755 Schneider, T., Lan, S., Stuart, A., & Teixeira, J. (2017). Earth system modeling
 756 2.0: A blueprint for models that learn from observations and targeted high-
 757 resolution simulations. *Geophysical Research Letters*, 44(24), 12,396–12,417.
 758 doi: 10.1002/2017GL076101
- 759 Schneider, T., Teixeira, J., Bretherton, C., Brient, F., Pressel, K., Schär, C., &
 760 Siebesma, A. (2017, 01). Climate goals and computing the future of clouds.
 761 *Nature Climate Change*, 7, 3–5. doi: 10.1038/nclimate3190
- 762 Schumann, U., & Sweet, R. A. (1988). Fast fourier transforms for direct solution
 763 of poisson’s equation with staggered boundary conditions. *Journal of Compu-
 764 tational Physics*, 75(1), 123 - 137. doi: [https://doi.org/10.1016/0021-9991\(88\)
 765 90102-7](https://doi.org/10.1016/0021-9991(88)90102-7)
- 766 Sokal, A. (1997). Monte carlo methods in statistical mechanics: Foundations
 767 and new algorithms. In C. DeWitt-Morette, P. Cartier, & A. Folacci (Eds.),
 768 *Functional integration: Basics and applications* (pp. 131–192). Boston, MA:
 769 Springer US. doi: 10.1007/978-1-4899-0319-8_6
- 770 Souza, A. (2020, Jul). *Uncertainty quantification of ocean parameterizations: Code
 771 and data.zip*. figshare. Retrieved from [https://figshare.com/articles/
 772 software/Uncertainty_quantification_of_ocean_parameterizations_Code
 773 _and_Data_zip/12743834/1](https://figshare.com/articles/software/Uncertainty_quantification_of_ocean_parameterizations_Code_and_Data_zip/12743834/1) doi: 10.6084/m9.figshare.12743834.v1
- 774 Sraj, I., Iskandarani, M., Thacker, W. C., Srinivasan, A., & Knio, O. M. (2014).
 775 Drag parameter estimation using gradients and hessian from a polyno-
 776 mial chaos model surrogate. *Monthly Weather Review*, 142(2), 933–941.
 777 Retrieved from <https://doi.org/10.1175/MWR-D-13-00087.1> doi:
 778 10.1175/MWR-D-13-00087.1
- 779 Sraj, I., Zedler, S. E., Knio, O. M., Jackson, C. S., & Hoteit, I. (2016). Polyno-
 780 mial chaos-based bayesian inference of k-profile parameterization in a general
 781 circulation model of the tropical pacific. *Monthly Weather Review*, 144(12),
 782 4621–4640. Retrieved from <https://doi.org/10.1175/MWR-D-15-0394.1> doi:
 783 10.1175/MWR-D-15-0394.1
- 784 Sullivan, P. P., & Patton, E. G. (2011, 10). The Effect of Mesh Resolution on
 785 Convective Boundary Layer Statistics and Structures Generated by Large-
 786 Eddy Simulation. *Journal of the Atmospheric Sciences*, 68(10), 2395-
 787 2415. Retrieved from <https://doi.org/10.1175/JAS-D-10-05010.1> doi:
 788 10.1175/JAS-D-10-05010.1
- 789 Thacker, W. C. (1989). The role of the hessian matrix in fitting models to mea-
 790 surements. *Journal of Geophysical Research: Oceans*, 94(C5), 6177–6196.
 791 Retrieved from [https://agupubs.onlinelibrary.wiley.com/doi/abs/
 792 10.1029/JC094iC05p06177](https://agupubs.onlinelibrary.wiley.com/doi/abs/10.1029/JC094iC05p06177) doi: 10.1029/JC094iC05p06177
- 793 Urrego-Blanco, J. R., Urban, N. M., Hunke, E. C., Turner, A. K., & Jeffery, N.
 794 (2016). Uncertainty quantification and global sensitivity analysis of the los
 795 alamos sea ice model. *Journal of Geophysical Research: Oceans*, 121(4), 2709-
 796 2732. Retrieved from [https://agupubs.onlinelibrary.wiley.com/doi/abs/
 797 10.1002/2015JC011558](https://agupubs.onlinelibrary.wiley.com/doi/abs/10.1002/2015JC011558) doi: 10.1002/2015JC011558
- 798 van Lier-Walqui, M., Vukicevic, T., & Posselt, D. J. (2012). Quantification of cloud
 799 microphysical parameterization uncertainty using radar reflectivity. *Monthly
 800 Weather Review*, 140(11), 3442–3466. Retrieved from [https://doi.org/
 801 10.1175/MWR-D-11-00216.1](https://doi.org/10.1175/MWR-D-11-00216.1) doi: 10.1175/MWR-D-11-00216.1
- 802 Van Roekel, L., Adcroft, A. J., Danabasoglu, G., Griffies, S. M., Kauffman, B.,
 803 Large, W., ... Schmidt, M. (2018). The kpp boundary layer scheme for the
 804 ocean: Revisiting its formulation and benchmarking one-dimensional simula-

- 805 tions relative to les. *Journal of Advances in Modeling Earth Systems*, 10(11),
 806 2647-2685. doi: 10.1029/2018MS001336
- 807 Verstappen, R. (2018). How much eddy dissipation is needed to counter-
 808 balance the nonlinear production of small, unresolved scales in a large-
 809 eddy simulation of turbulence? *Computers & Fluids*, 176, 276–284. doi:
 810 10.1016/j.compfluid.2016.12.016
- 811 Vreugdenhil, C. A., & Taylor, J. R. (2018). Large-eddy simulations of stratified
 812 plane Couette flow using the anisotropic minimum-dissipation model. *Physics*
 813 *of Fluids*, 30(8), 085104. doi: 10.1063/1.5037039
- 814 Wang, D., Large, W. G., & McWilliams, J. C. (1996). Large-eddy simulation of the
 815 equatorial ocean boundary layer: Diurnal cycling, eddy viscosity, and horizon-
 816 tal rotation. *Journal of Geophysical Research: Oceans*, 101(C2), 3649-3662.
 817 Retrieved from [https://agupubs.onlinelibrary.wiley.com/doi/abs/](https://agupubs.onlinelibrary.wiley.com/doi/abs/10.1029/95JC03441)
 818 10.1029/95JC03441 doi: 10.1029/95JC03441
- 819 Wunsch, C. (2006). *Discrete inverse and state estimation problems: With geo-*
 820 *physical fluid applications*. Cambridge University Press. doi: 10.1017/
 821 CBO9780511535949
- 822 Zedler, S. E., Kanschä, G., Korty, R., & Hoteit, I. (2012). A new approach for
 823 the determination of the drag coefficient from the upper ocean response to a
 824 tropical cyclone: a feasibility study. *Journal of Oceanography*, 68(2), 227–
 825 241. Retrieved from <https://doi.org/10.1007/s10872-011-0092-6> doi:
 826 10.1007/s10872-011-0092-6